

CANCER

Cellular Trojan Horse initiates bimetallic Fe-Cu MOF-mediated synergistic cuproptosis and ferroptosis against malignancies

Kerong Chen^{1†}, Anwei Zhou^{2†}, Xinyuan Zhou¹, Jielei He¹, Yurui Xu^{1*}, Xinghai Ning^{1*}

Disruptions in metal balance can trigger a synergistic interplay of cuproptosis and ferroptosis, offering promising solutions to enduring challenges in oncology. Here, we have engineered a Cellular Trojan Horse, named MetaCell, which uses live neutrophils to stably internalize thermosensitive liposomal bimetallic Fe-Cu MOFs (Lip@Fe-Cu-MOFs). MetaCell can instigate cuproptosis and ferroptosis, thereby enhancing treatment efficacy. Mirroring the characteristics of neutrophils, MetaCell can evade the immune system and not only infiltrate tumors but also respond to inflammation by releasing therapeutic components, thereby surmounting traditional treatment barriers. Notably, Lip@Fe-Cu-MOFs demonstrate notable photothermal effects, inciting a targeted release of Fe-Cu-MOFs within cancer cells and amplifying the synergistic action of cuproptosis and ferroptosis. MetaCell has demonstrated promising treatment outcomes in tumor-bearing mice, effectively eliminating solid tumors and forestalling recurrence, leading to extended survival. This research provides great insights into the complex interplay between copper and iron homeostasis in malignancies, potentially paving the way for innovative approaches in cancer treatment.

INTRODUCTION

Metal ions play an essential role in maintaining cellular functions and overall organism health, necessitating a precise balance within cells to ensure proper biological function and avert harmful effects (1, 2). An imbalance in cellular levels of metal ions such as iron (Fe), copper (Cu), zinc (Zn), and magnesium (Mg) can lead to a myriad of pathological conditions, with an increased risk of cancer being especially noteworthy (3–8). It has been shown that, compared to normal cells, cancer cells often adapt and elevate their requirement for metal ions to sustain their hyperactive metabolism, thus making metal homeostasis a promising target for cancer therapy (9–11). Disrupting metal ion homeostasis can yield a range of therapeutic benefits. Such disruptions can directly instigate cancer cell death and effectively hinder cell survival processes. In addition, these disruptions have the potential to overcome resistance mechanisms inherent to cancer cells, thereby improving the effectiveness of cancer treatments (12, 13). Therefore, the exploration of metal ion homeostasis is a crucial facet of research for enhancing our understanding of malignancies and for the development of innovative therapeutic strategies.

Recent substantial advancements in our understanding of metal ion homeostasis have paved the way for the exploration and development of advanced therapeutic strategies to enhance cancer treatment (14, 15). In particular, copper and iron, recognized as vital trace elements required for a myriad of biological processes, have been thrust into the spotlight of these investigations (16, 17). The

human body has evolved complex mechanisms to regulate and maintain the homeostasis of these trace elements. However, imbalances in intracellular copper and iron levels can instigate cell death via unique mechanisms such as cuproptosis and ferroptosis (18, 19). Distinct from conventional types of programmed cell death, including necrosis, apoptosis, and autophagy, cuproptosis and ferroptosis represent newly recognized forms of cell death with unique characteristics and metal ion-dependent oxidative stress mechanisms (20, 21). Cuproptosis is a copper-induced cell death process, precipitated by excessive intracellular copper accumulation. This results in the aggregation of lipoylated dihydrolipoamide S-acetyltransferase (DLAT) and disruption of the mitochondrial tricarboxylic acid (TCA) cycle, culminating in proteotoxic stress and consequent cell death (22). On the other hand, ferroptosis is an iron-dependent form of programmed cell death characterized by the accumulation of lipid peroxidation products, leading to membrane destabilization and, ultimately, cell death (23). Consequently, cuproptosis and ferroptosis represent distinct cell death processes, each with unique metal ion dependencies and biological mechanisms. To fully leverage their potential in cancer treatment, additional research is required to enrich our understanding of their molecular mechanisms and optimize therapeutic strategies.

A growing body of research is exploring the utilization of cuproptosis and ferroptosis to enhance cancer treatment, capitalizing on their unique therapeutic attributes to overcome drug resistance and minimize side effects (24, 25). Despite divergent primary triggers and mechanisms, cuproptosis and ferroptosis share several commonalities in their associations with various pathological conditions, such as oxidative stress, abnormal metabolism, and disruption of cellular processes. Moreover, both have implications in the development and progression of cancer, underscoring the potential intersection of cuproptosis and ferroptosis as promising therapeutic targets for future research and drug development (26, 27). Of substantial note, the synergistic induction of cuproptosis and ferroptosis could overcome certain limitations of standalone therapies, such

Copyright © 2024 The Authors, some rights reserved; exclusive licensee American Association for the Advancement of Science. No claim to original U.S. Government Works. Distributed under a Creative Commons Attribution NonCommercial License 4.0 (CC BY-NC).

¹National Laboratory of Solid State Microstructures, Collaborative Innovation Center of Advanced Microstructures, Chemistry and Biomedicine Innovation Center, College of Engineering and Applied Sciences, Jiangsu Key Laboratory of Artificial Functional Materials, Nanjing University, Nanjing 210093, P. R. China. ²National Laboratory of Solid State Microstructures, Collaborative Innovation Center of Advanced Microstructures, Chemistry and Biomedicine Innovation Center, School of Physics, Jiangsu Key Laboratory of Artificial Functional Materials, Nanjing University, Nanjing 210093, P. R. China.

*Corresponding author. Email: xuyurui@nju.edu.cn (Y.X.); xning@nju.edu.cn (X.N.)

†These authors contributed equally to this work.

as drug resistance or restricted efficacy (28, 29). This synergistic effect could be particularly pronounced when both iron and copper accumulate excessively, leading to an elevation in reactive oxygen species (ROS) (30, 31). The ensuing increase in oxidative stress can escalate cellular damage and potentiate cell death, thereby exerting a more robust anticancer effect than either cuproptosis or ferroptosis alone (32, 33). Nonetheless, research into the concurrent activation of these two cell death mechanisms remains limited, as cuproptosis and ferroptosis have largely been investigated independently.

In this work, we introduce a multifunctional cellular Trojan Horse (referred to as MetaCell), designed to concurrently activate cuproptosis and ferroptosis. This approach aims to circumvent drug resistance, enhance treatment efficacy, and minimize side effects (Fig. 1A).

MetaCell comprises live neutrophils that encapsulate a thermosensitive liposomal formulation of bimetallic Fe-Cu metal-organic frameworks (Lip@Fe-Cu-MOFs). The generation of MetaCell uses an integrated fabrication strategy, resulting in a responsive therapeutic platform with distinct properties. Fe-Cu-MOFs are synthesized by integrating iron and copper metal ions with organic ligands to form a highly porous framework. These bimetallic Fe-Cu-MOFs exhibit superior properties compared to their monometallic counterparts, including enhanced stability, elevated catalytic activity, and augmented adsorption capacity. To further enhance the effectiveness of Fe-Cu-MOFs, they are encapsulated within thermosensitive liposomes, which are subsequently internalized by live neutrophils. This biomimetic approach imparts MetaCell with inherent neutrophil

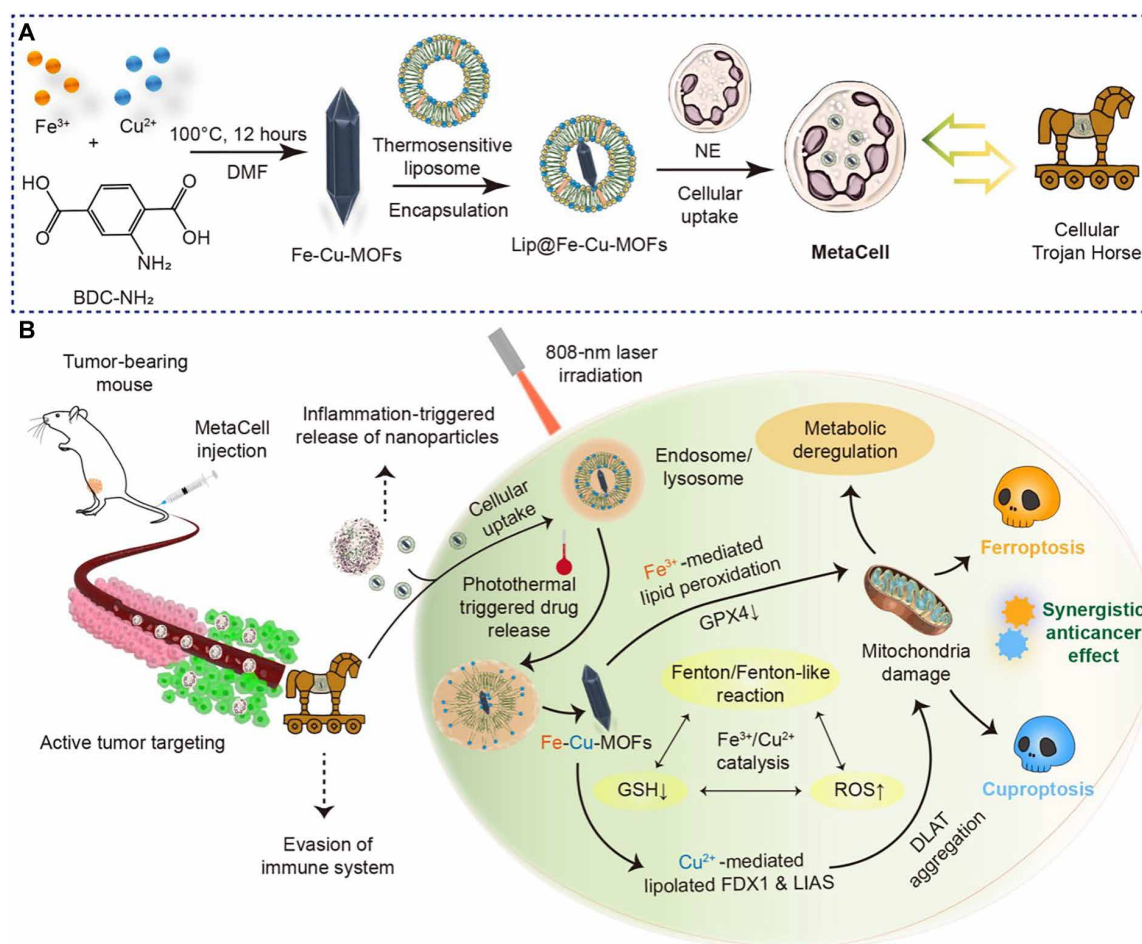


Fig. 1. An innovative cellular Trojan Horse strategy uses synergistic cuproptosis and ferroptosis for targeted cancer intervention. (A) Design and preparation of cellular Trojan Horse (MetaCell). MetaCell comprises live neutrophils encapsulating a thermosensitive liposomal formulation of bimetallic Lip@Fe-Cu-MOFs. This innovative construct is created through an integrated fabrication strategy where Fe-Cu-MOFs are first synthesized by coordinating iron and copper metal ions with organic ligands, forming a well-defined porous framework. The Fe-Cu-MOFs are then incorporated within thermosensitive liposomes and subsequently internalized by live neutrophil (NE). This biomimetic approach endows MetaCell with a range of inherent neutrophil properties, resulting in a plethora of advantages. (B) A schematic illustration depicting the synergistic anticancer effects of cuproptosis and ferroptosis triggered by MetaCell. Taking advantage of the unique properties of neutrophils, MetaCell is designed to effectively evade the immune system. It not only infiltrates tumors but also responds to inflammation, releasing therapeutic components. This unique feature enables MetaCell to overcome traditional treatment barriers, notably enhancing its cancer treatment potential. In addition, MetaCell is programmed to respond to inflammation, instigating the release of Lip@Fe-Cu-MOFs within tumor. Once internalized, these thermosensitive liposomes discharge Fe-Cu-MOFs when exposed to NIR light, capitalizing on their potent photothermal properties. Moreover, photothermal heating not only stimulates the release of Fe-Cu-MOFs within cancer cells but also amplifies the simultaneous activation of cuproptosis and ferroptosis mediated by Fe-Cu-MOFs. By orchestrating this synergistic cell death, MetaCell targets diverse aspects of cancer biology, thereby enhancing therapeutic potency and substantially reducing the likelihood of cancer recurrence.

characteristics, providing a range of benefits such as improved biocompatibility, immune system evasion, and targeted delivery. MetaCell is uniquely engineered to facilitate tumor-targeted release in response to inflammatory stimuli induced by multiple near-infrared (NIR) laser irradiations. The enhanced inflammation level in tumor tissues, as opposed to normal tissues, leads to a more substantial accumulation of MetaCell and release of Lip@Fe-Cu-MOFs, culminating in a self-amplifying tumor-targeting effect. Furthermore, the deliberate application of NIR laser stimulation exclusively to tumor regions, not normal tissues, creates notable inflammation differentials. These differentials are instrumental in augmenting the recruitment of MetaCell to tumor sites, thereby increasing the content of Lip@Fe-Cu-MOFs within tumor cells. This mechanism paves the way for the potential anticancer efficiency of MetaCell, leveraging the synergistic effect of metal homeostasis and photothermal therapy (PTT). As a result, MetaCell can infiltrate and target cancer cells, thus enhancing the overall efficacy of cancer treatment.

Upon cellular uptake, the thermosensitive liposomes are designed to discharge their drug payload upon exposure to a specific temperature. This characteristic can be leveraged for controlled drug release via localized heating of the tumor region, a process made possible through photothermal effects (34). This dual-responsive mechanism ensures the accumulation of therapeutic agents within the tumor site, thereby boosting treatment efficacy. Notably, Fe-Cu-MOFs exhibit substantial photothermal conversion capabilities due to their strong absorbance in the NIR region, which allows for the generation of localized heat upon NIR light irradiation. This attribute not only facilitates MetaCell-mediated photothermal heating for the release of Fe-Cu-MOFs within cancer cells but also amplifies the concurrent induction of cuproptosis and ferroptosis facilitated by Fe-Cu-MOFs. The Fenton/Fenton-like reaction, capable of being catalyzed by Fe^{3+} or Cu^{2+} , plays a pivotal role in generating hydroxyl radicals. These radicals, in conjunction with Cu^{2+} , orchestrate a depletion of glutathione (GSH) within tumor cells. This coordinated action synergistically induces both ferroptosis and cuproptosis, highlighting a complex interplay of cellular processes. By driving this synergistic action of cuproptosis and ferroptosis, MetaCell targets multiple aspects of cancer biology, thereby increasing treatment potency and reducing the likelihood of cancer recurrence. Consequently, we have conducted a systematic investigation of the potential benefits, optimal delivery strategies, and possible side effects of combined cuproptosis and ferroptosis as a cancer therapy, both *in vitro* and *in vivo* (Fig. 1B). In exploring the potential of cuproptosis and ferroptosis in cancer treatment, this study lays the groundwork for innovative therapeutic strategies that exploit the vulnerabilities of cancer cells. This strategy results in enhanced treatment efficacy, effectively tackling the complexities and challenges associated with cancer therapy.

RESULTS

Preparation and characterization of Lip@Fe-Cu-MOFs

Metal homeostasis refers to the intricate modulation and equilibrium of metal ions within a living entity. Specific metals, termed as biometals, are indispensable for the sustenance of life. These encompass elements such as iron, copper, zinc, magnesium, and manganese among others. They hold an integral part in numerous biological processes, from the catalysis of enzymes, mediation of signal transduction, to the regulation of gene expression (1)

However, these essential biometals could transmute into deleterious agents if not accurately managed. This stems from the propensity of metal ions to participate in redox reactions, engendering ROS. These ROS can induce oxidative stress and inflict harm on cellular constituents (35). As such, strategies targeting the modulation of metal homeostasis show immense potential in various sectors of biomedical research and therapeutics. Intriguingly, recent studies depict that disruptions in the intracellular concentrations of copper and iron can catalyze a joint mechanism of cuproptosis and ferroptosis (28, 36). This synergistic phenomenon offers a progressive approach to address multiple challenges associated with cancer therapy.

In a pursuit to augment cancer treatment efficacy through the coordinated induction of cuproptosis and ferroptosis, we engineered an intelligent therapeutic construct, termed as MetaCell. This platform consists of live neutrophils encapsulating a thermosensitive liposomal formulation of bimetallic Lip@Fe-Cu-MOFs, which were assembled via an integrative fabrication process. The first stage involved the hydrothermal synthesis of Fe-Cu-MOFs demonstrating a polyhedral structure. The optimization of synthesis parameters such as temperature, reaction duration, pH, and molar ratios ensured the production of Fe-Cu-MOFs with desired properties. In particular, a combined aqueous solution of $\text{FeCl}_3 \cdot 6\text{H}_2\text{O}$ and $\text{CuCl}_2 \cdot 2\text{H}_2\text{O}$ was incorporated into a *N,N'*-dimethylformamide (DMF) solution containing 2-Aminoterephthalic acid (NH_2 -BDC), generating a uniform mixture. Here, $\text{FeCl}_3 \cdot 6\text{H}_2\text{O}$ and $\text{CuCl}_2 \cdot 2\text{H}_2\text{O}$ functioned as metal salt precursors, undergoing a reaction with NH_2 -BDC to establish coordination bonds and thus form a MOF structure. The molar ratios of metal ions to ligands were fine-tuned in accordance with the preferred composition of the Fe-Cu-MOFs. In addition, the reaction mixture underwent heating to a defined temperature for a specified duration, which could influence the final morphology of the Fe-Cu-MOFs. After the hydrothermal reaction, the mixture was allowed to naturally cool to room temperature, subsequent to which the precipitated Fe-Cu-MOF crystals were diligently collected via filtration or centrifugation techniques.

A suite of analytical techniques was used to characterize the synthesized Fe-Cu-MOFs, validating their structure and morphology. These included transmission electron microscopy (TEM), x-ray diffraction (XRD), inductively coupled plasma mass spectrometry (ICP-MS), and scanning electron microscopy (SEM)-energy dispersive spectroscopy (EDS). As observed from the TEM image, Fe-Cu-MOFs display a spindle-like polyhedron morphology. These particles show an average diameter of approximately 50 nm and an average length of approximately 200 nm (Fig. 2A). XRD analysis was also performed to decipher the crystal structure of the MOFs. The obtained XRD spectra of Fe-Cu-MOFs are depicted in fig. S1, validating the successful synthesis of Fe-Cu-MOFs and appropriate integration of Fe atoms into the MOF architecture. Complementarily, we executed ICP-MS characterization to quantify the elemental content of Fe and Cu in Fe-Cu-MOFs. This technique offers the ability to detect and measure trace elements and isotopes across a broad range of sample matrices. ICP-MS analysis indicated a substantial enrichment of Fe and Cu within the Fe-Cu-MOFs, quantifying Fe at 21% and Cu at 5% of the overall elemental composition. Moreover, SEM-EDS analysis displays an evenly dispersed distribution of Fe and Cu atoms throughout the MOFs, with the ratio between Fe and Cu content being approximately 4.72:1 (fig. S2). This observation substantiates the successful fabrication of Fe-Cu-MOFs with a homogeneous allocation of metal atoms.

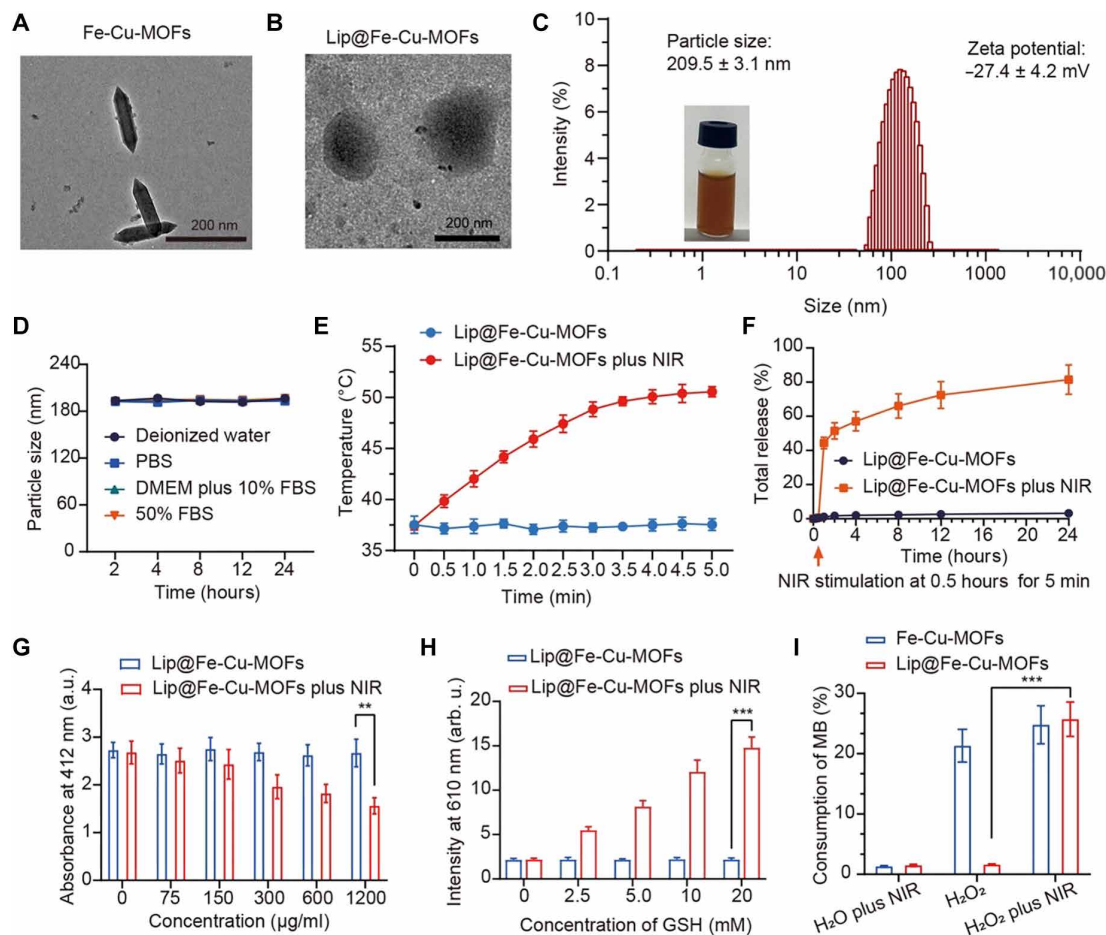


Fig. 2. Synthesis and characterization of Lip@Fe-Cu-MOFs. (A) TEM images of Fe-Cu-MOFs. Scale bar, 200 nm. (B) TEM images of Lip@Fe-Cu-MOFs. Scale bar, 200 nm. (C) The size distribution and zeta potential of Lip@Fe-Cu-MOFs, measured by DLS. (D) Dynamic stability of Lip@Fe-Cu-MOFs. Measurement was tested in deionized water, phosphate-buffered saline (PBS), Dulbecco's modified Eagle's medium (DMEM) with 10% fetal bovine serum (FBS), and 50% FBS, which was kept at 37°C for 48 hours. (E) Photothermal effects of Lip@Fe-Cu-MOFs. The temperature increasing profiles of Lip@Fe-Cu-MOFs was measured under NIR laser stimulation (808 nm, 1.5 W/cm²) for 5 min. (F) The time-dependent release of C6-labeled Fe-Cu-MOFs from Lip@Fe-Cu-MOFs_{C6} under specific conditions. The experimental setup assessed the release kinetics with and without the application of NIR stimulation (808 nm, 1.5 W/cm²) over a period of 5 min. The quantitative data reflecting the C6-labeled Fe-Cu-MOFs release was systematically recorded. (G) Lip@Fe-Cu-MOF-mediated GSH depletion, measured by the 5,5'-dithiobis-(2-nitrobenzoic acid) (DTNB) assay. (H) Evaluation of Cu⁺ Generation. Lip@Fe-Cu-MOFs were incubated with various concentrations of GSH. Subsequently, the fluorescence intensity at a wavelength of 610 nm was measured, using an excitation wavelength of 365 nm. (I) Assessment of Lip@Fe-Cu-MOF-catalyzed Fenton-like reaction. The methylene blue (MB) assay was used to examine the catalytic capability of Lip@Fe-Cu-MOFs in promoting the Fenton-like reaction. This was conducted under NIR stimulation at 808 nm, with an intensity of 1.5 W/cm² for a duration of 5 min. Data are presented as mean \pm SD, with $n = 3$. ** $P < 0.01$ and *** $P < 0.001$ (Student's t test, two tails). a.u., absorbance units; arb. u., arbitrary units.

Despite the potential therapeutic advantages of Fe-Cu-MOFs, we endeavored to further elevate their therapeutic capacity by encapsulating them within thermosensitive liposomes. These liposomes represent a class of temperature-responsive drug delivery systems, meticulously designed to release their therapeutic payload at a designated temperature threshold, typically surpassing physiological body temperature (approximately 50°C) (37). For instance, the liposomes, assembled from soybean phosphatidylcholine (PC), 1,2-dipalmitoyl-sn-glycero-3-phosphocholine (DPPC), cholesterol, and distearoyl phosphoethanolamine-polyethylene glycol, molecular weight 2000 (DSPE-PEG2000), exhibit a low phase transition temperature (T_m) of about 43°C, thus promoting this formulation as an auspicious drug carrier (38). Accordingly, we furnished Fe-Cu-MOFs with a coating of thermosensitive liposomes, thereby generating Lip@Fe-Cu-MOFs. Dynamic light scattering (DLS) analyses

indicate that Lip@Fe-Cu-MOFs had an average hydrodynamic diameter of 209.5 ± 3.1 nm and a zeta potential of -27.4 ± 4.2 mV (Fig. 2B). It is well-established that nanoparticles bearing a negative charge often exhibit enhanced colloidal stability and diminished propensity for aggregation (38). Such ideal characteristics, inclusive of the negative charge and nanoparticle sizing, render Lip@Fe-Cu-MOFs well-suited for both *in vitro* and *in vivo* applications. Moreover, TEM imagery affirms that Lip@Fe-Cu-MOFs constituted a well-dispersed nanoparticle with a core diameter of roughly 180 nm (Fig. 2C). SEM-EDS analysis verified the presence of Fe and Cu atoms in Lip@Fe-Cu-MOFs, with Fe and Cu constituting 5.38 and 1.03%, respectively (refer to fig. S12). Complementing this, x-ray photoelectron spectroscopy (XPS) characterization revealed distinct peaks at 724.58 and 710.98 eV, attributable to Fe2p_{1/2} and Fe2p_{3/2}. For Cu, the Cu 2p XPS demonstrated peaks at 954.22 eV

(Cu 2p_{1/2}) and 931.54 eV (Cu 2p_{3/2}), accompanied by pronounced satellite peaks at approximately 962 and 943 eV. These findings collectively confirm the presence of Fe³⁺ and Cu²⁺ in Lip@Fe-Cu-MOFs structure (see fig. S13). It should be noted that nanoparticle stability can be influenced by a plethora of factors such as the type of media, pH, temperature, and storage conditions (39). Consequently, it is prudent to undertake stability testing under conditions mirroring their intended application. As shown in Fig. 2D, Lip@Fe-Cu-MOFs maintained their stability for at least 24 hours at 37°C in diverse environments. This indicates their potential robustness for in vivo applications, with minimal degradation or loss of efficacy.

Photothermal responsiveness of Lip@Fe-Cu-MOFs

Creating thermosensitive drug delivery systems requires the meticulous optimization of the material composition and formulation. This ensures temperature sensitivity, efficient drug encapsulation, and controlled release kinetics (40). In this work, we have enhanced the biocompatibility of Fe-Cu-MOFs by cloaking them with thermosensitive liposomes, which also endows them with temperature-triggered drug release capabilities. The thermosensitive lipid used undergoes a phase transition at a specific temperature, enabling the release of encapsulated drugs into targeted tissues (41). Our primary investigation involved assessing the photothermal effect of Lip@Fe-Cu-MOFs. The photothermal heating curves of Lip@Fe-Cu-MOFs, observed under 808-nm light stimulation (1.5 W/cm²), revealed significant photothermal behavior. As shown in Fig. 2E, the temperature of Lip@Fe-Cu-MOFs, containing Fe-Cu-MOFs (500 µg/ml), rose to ~50°C after 5 min of irradiation. This indicates that Lip@Fe-Cu-MOFs have a substantial photothermal conversion capacity.

In addition, we monitored the time-dependent release of coumarin 6 (C6) from C6-labeled Lip@Fe-Cu-MOFs (Lip@Fe-Cu-MOFs_{C6}), in which a Lip@Fe-Cu-MOFs_{C6} solution was irradiated with an 808-nm laser (1.5 W/cm²) for 5 min. Figure 2F reveals that NIR laser irradiation triggered the 44.36% release of C6, which was rapidly liberated from Lip@Fe-Cu-MOFs_{C6} within 1 hour after 5-min 808-nm laser stimulation. Samples that did not undergo laser stimulation showed a negligible release of C6. These findings suggest that Lip@Fe-Cu-MOFs have the potential to deliver therapeutic payloads into tumors while preserving biosafety in healthy tissues that have not undergone NIR laser stimulation. Thus, Lip@Fe-Cu-MOFs can be engineered to release their payload at specific temperatures, thereby providing precision control over drug release at the tumor site. This mechanism limits the exposure of healthy tissues to the therapeutic agents, which consequently reduces potential side effects.

Catalytic activity of Lip@Fe-Cu-MOFs

The development of MOFs that can effectively initiate synergistic cuproptosis and ferroptosis could revolutionize cancer treatment by circumventing drug resistance and simultaneously targeting multiple cancer cell vulnerabilities (42, 43). In this study, we designed bimetallic MOFs laden with both copper and iron ions to manipulate intracellular redox stress. Accumulating evidence suggests that GSH acts not only as a natural ROS scavenger but also as an intracellular copper chaperone, thus providing protection to cancer cells against oxidative damage (25, 44). Therefore, rapidly depleting GSH seems a promising approach for disrupting intracellular redox homeostasis. Lip@Fe-Cu-MOFs can achieve intracellular codelivery of Fe³⁺ and Cu²⁺, which subsequently induces the generation of ROS and

directly depletes GSH. This approach holds therapeutic potential for cancer treatment. However, it is crucial to note that using ROS as a therapeutic strategy comes with potential risks and limitations that must be meticulously assessed.

We therefore conducted an in-depth analysis of the capacity of Lip@Fe-Cu-MOFs to deplete GSH by deploying 5,5'-dithiobis-(2-nitrobenzoic acid) (DTNB) or Ellman's reagent, which is a widely used compound in biochemistry and molecular biology due to its reactivity with thiol groups. DTNB, upon encountering a sample with free SH groups, initiates a reaction to form TNB (2-nitro-5-thiobenzoic acid). This resulting compound has a yellow color with an absorption at 412 nm. The degree of yellow color intensity directly corresponds to the free SH group concentration present within the sample. In our investigation, as presented in Fig. 2G, Lip@Fe-Cu-MOFs brought about a reduction in TNB's absorbance, hinting at a possible catalytic role of Fe and Cu in the degradation of GSH. Significantly, a higher concentration of Lip@Fe-Cu-MOFs produced a more decrease in TNB's absorbance, thereby confirming the capability of Lip@Fe-Cu-MOFs to consume GSH. The proficiency of Lip@Fe-Cu-MOFs in depleting GSH is intricately tied to the redox pairs of copper ions (Cu⁺ and Cu²⁺), wherein Cu²⁺ is reducible to Cu⁺ by GSH. Acting as a reducing agent, GSH donates electrons to Cu²⁺, leading to its conversion to Cu⁺ ions. We verified the generation of Cu⁺ instigated by GSH via fluorescence spectroscopy. When GSH interacted with Lip@Fe-Cu-MOFs, an upsurge in the emission intensity at 610 nm was observed (Fig. 2H), confirming the reduction of Cu²⁺ to Cu⁺ during GSH depletion. This occurrence is noteworthy as Cu⁺ ions are known to emit light at a wavelength of 610 nm. The validation of the ability of Lip@Fe-Cu-MOFs to deplete GSH and facilitate the reduction of Cu²⁺ to Cu⁺ ions underscores its potential for disrupting intracellular redox homeostasis, providing a promising avenue for therapeutic strategies against cancer.

The redox activity of Lip@Fe-Cu-MOFs could contribute to GSH depletion by generating ROS, which can oxidize GSH, forming oxidized glutathione (GSSG). Previous studies have established that MOFs containing Fe ions can catalyze the Fenton reaction, leading to the generation of ROS, notably hydroxyl radicals (·OH) (45). These highly reactive radicals can inflict oxidative damage on biomolecules. Notably, GSH is critical for neutralizing hydroxyl radicals, which can cause a depletion of cellular GSH levels, thereby escalating the vulnerability of cells to oxidative damage (46). With this understanding, we explored their capability to instigate the Fenton reaction through the methylene blue (MB) assay. A mixed solution of H₂O₂ (1 mM) and MB was exposed to laser irradiation (808 nm, 1.5 W/cm²) for 5 min in the presence of either Lip@Fe-Cu-MOFs or Fe-Cu-MOFs, after which the absorbance reading at 664 nm was recorded. As depicted in Fig. 2I, Fe-Cu-MOFs demonstrated a remarkable ability to catalyze the Fenton reaction, thereby oxidizing and degrading MB. This confirms that Fe-Cu-MOFs are highly effective catalysts. Without NIR laser irradiation, Lip@Fe-Cu-MOFs did not exhibit catalytic activity, likely due to the liposomal coating acting as a physical barrier, limiting the interaction of Fe-Cu-MOFs with H₂O₂ and restricting their catalytic potential. However, under NIR irradiation, Lip@Fe-Cu-MOFs showcased notable catalytic behaviors, rapidly consuming more than 20% of MB, hence confirming its photoactive responsiveness. In essence, Lip@Fe-Cu-MOFs are a responsive catalyst capable of triggering the Fenton reaction in a controlled manner,

potentially a beneficial attribute for cancer treatment. It allows for the activity to be regulated, avoiding undesired reactions against healthy tissues.

Preparation and characterization of MetaCell

Both organic and inorganic materials used in drug delivery systems can present challenges regarding immunogenicity and toxicity, which may elicit undesired side effects (47). Using endogenous cells that come from the patient's own body could potentially circumvent these issues, making them an appealing alternative for drug delivery (48). Thanks to their host attributes, these cells could offer unique biological effects or targeting abilities, paving the way for next-generation personalized medicine (49). Recent advancements in biological and medical sciences have spotlighted neutrophils as potential candidates for drug delivery systems (50). Despite their promise, neutrophils as drug carriers come with inherent limitations. Their relatively short lifespan, potential for eliciting unintended immune responses, and variability in performance due to the patient's health status can affect their effectiveness. Moreover, neutrophils, in their natural state, might not be equipped to address the multifaceted nature of tumor environments. This limitation necessitates the development of innovative, multifunctional cellular therapeutics (51). By leveraging nanoengineering techniques, we can enhance the intrinsic properties of neutrophils, thereby tailoring them to meet the specific demands of complex tumor treatments. These advancements could transform neutrophils into more efficient, targeted, and adaptive carriers, capable of navigating and responding to the dynamic and often hostile tumor microenvironment.

In this study, we created MetaCell by encapsulating Lip@Fe-Cu-MOFs within live neutrophils. As depicted in Fig. 3A and fig. S19, Lip@Fe-Cu-MOFs exhibited negligible toxicity toward neutrophils following a 12-hour incubation at varying concentrations. In addition, microscopy images reveal no significant changes in neutrophil morphology post-encapsulation (Fig. 3B). Given the pivotal role of inflammation recruitment in neutrophils during the innate immune response, we delved into the chemotaxis-associated biomarkers in MetaCell. As illustrated in fig. S7, both neutrophils and MetaCell exhibited analogous CD11b expression levels, signifying that MetaCell retains its resting state even after being encapsulated with Lip@Fe-Cu-MOFs. Moreover, an increase in CD11b expression was detected in MetaCell posttreatment with 100 nM *N*-formylmethionyl-leucyl-phenyl-alanine (fMLP) for a duration of 0.5 hours, highlighting MetaCell's potential to be activated by inflammatory stimuli. Moreover, our transwell migration assay suggests that MetaCell retained the fMLP-activated chemotactic behavior typical of neutrophils (Fig. 3C). This suggests that our nanoengineering approach has no impact on cell viability. Furthermore, we evaluated the cellular uptake of C6-labeled Lip@Fe-Cu-MOFs in neutrophils using flow cytometry. Figure 3 (D and E) demonstrates the rapid accumulation of Lip@Fe-Cu-MOFs in neutrophils, reaching the highest uptake at 2 hours. Confocal imaging further reveals that Lip@Fe-Cu-MOFs, indicated by green fluorescence, were evenly distributed throughout the neutrophil cytoplasm.

In addition, we used another approach to assess the stability of Lip@Fe-Cu-MOFs within MetaCell. 1,1'-Diiodo-3,3',3'-tetra-methylindocarbocyanine perchlorate (DiI)-labeled thermosensitive liposomes were used to encapsulate fluorescein isothiocyanate (FITC)-labeled Fe-Cu-MOFs. These double fluorescence-labeled constructs were then taken up by neutrophils to form MetaCell. The

colocalization and stability of these fluorescent markers within MetaCell were characterized using a confocal laser scanning microscope (CLSM; FV3000, Olympus, Japan). Our findings, as depicted in fig. S14, demonstrated a notable colocalization of DiI and FITC within MetaCell for up to 12 hours. This observation suggests a high degree of storage stability for Lip@Fe-Cu-MOFs inside MetaCell. Despite the relatively short lifespan of neutrophils, which typically spans 18 to 24 hours, the capacity of MetaCell to maintain the integrity of Lip@Fe-Cu-MOFs without obvious degradation or loss during this timeframe is a promising indicator of its potential efficacy in therapeutic contexts. This attribute underscores the viability of MetaCell as a transient yet effective delivery system for targeted cancer treatment.

The encapsulation efficiency of Fe-Cu-MOFs within MetaCell was quantitatively evaluated using ICP-MS. The results of this analysis indicated that around 1×10^7 MetaCells incorporated approximately 102.33 μg of iron (Fe) and 22.86 μg of copper (Cu). This elemental distribution equates to approximately 500 μg of Fe-Cu-MOF, thereby confirming efficient cellular uptake and internalization. We further investigated the stability and release profile of Lip@Fe-Cu-MOFs within MetaCell during the chemotactic process. Under physiological conditions, Lip@Fe-Cu-MOFs were retained within neutrophils for up to 6 hours, with minimal release. However, when incubated with phorbol-12-myristate-13-acetate (PMA), a compound often used for promoting oxidative stress and inflammation, we observed a burst release of Fe after 3 hours (Fig. 3F). These findings suggest that Lip@Fe-Cu-MOFs preserve the physiological functions of neutrophils, enabling them to respond actively to inflammatory stimuli and migrate directionally toward inflammation sites.

Tumor-targeted delivery of MetaCell

Neutrophils, crucial components of the innate immune system, are traditionally known for their ability to combat infections through phagocytosis, degranulation, and the formation of neutrophil extracellular traps (52). In the context of cancer, neutrophils can infiltrate tumors and interact with other cells in the tumor microenvironment, endowing them with tumor-targeting abilities (53). However, this process is not always specific and can lead to nonspecific accumulation in nontumorous tissues. Such nonspecific accumulation can potentially result in off-target effects and may contribute to inflammation or even tissue damage in areas not affected by the cancer (54). This behavior underlines the complexity of using neutrophils in cancer therapy and highlights the need for enhanced targeting strategies to ensure that their tumor-fighting capabilities are effectively and precisely used against malignant cells, minimizing collateral impact on healthy tissues.

To overcome the inherent limitations of neutrophils and ensure selective delivery of therapeutics to tumor tissues while protecting normal cells, we have intricately designed MetaCell with a self-amplifying tumor-targeting mechanism. MetaCell is precision-engineered to react to inflammatory signals specifically in tumor areas, which are amplified by multiple NIR laser irradiations. This precise application of NIR laser stimulation exclusively to tumor regions, as opposed to normal tissues, creates a substantial disparity in inflammatory responses. This enhanced inflammation is crucial in boosting MetaCell's accumulation predominantly at tumor sites, effectively concentrating the therapeutic Lip@Fe-Cu-MOFs within cancer cells. Leveraging the innate tumor-homing capability of

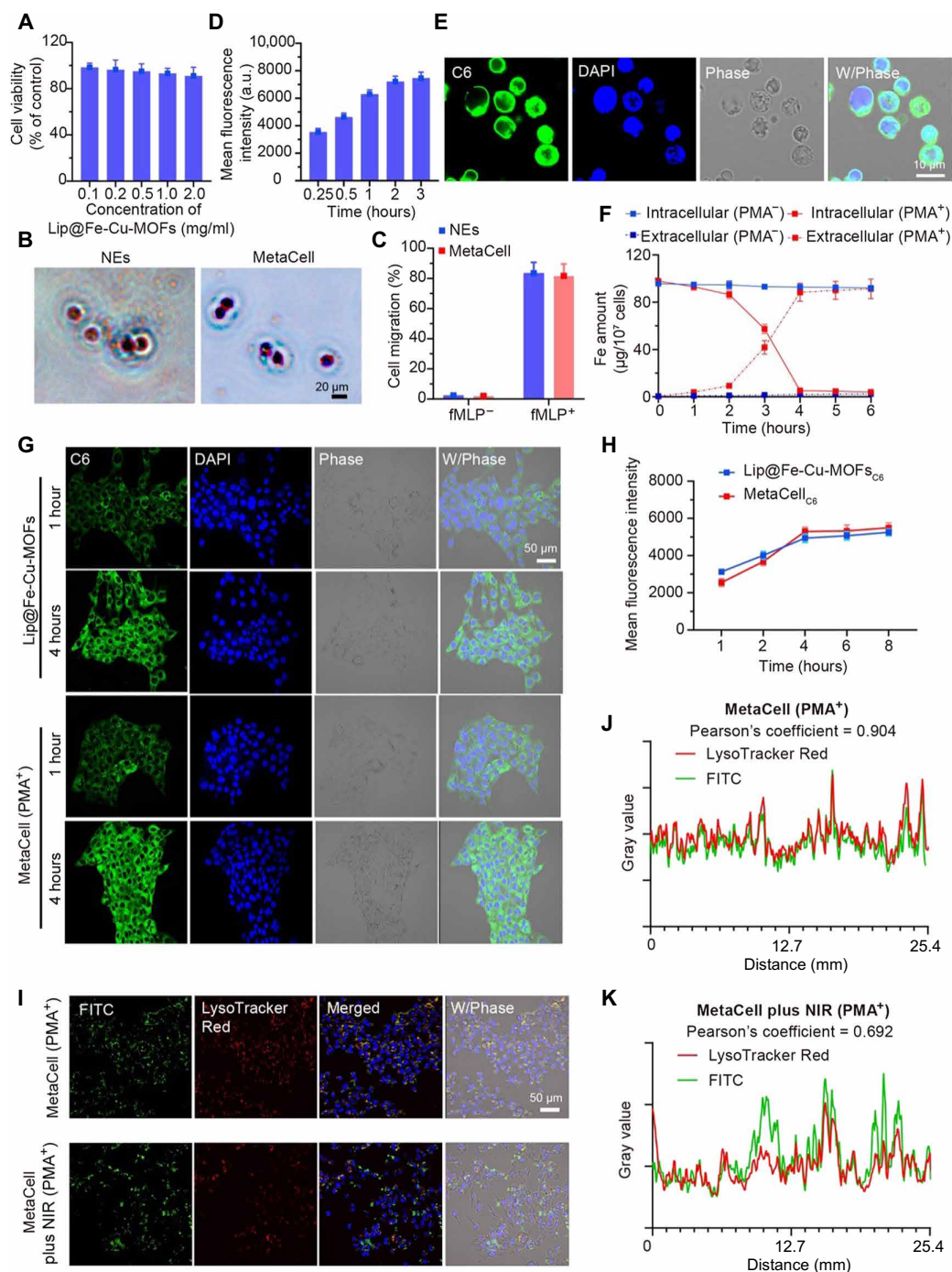


Fig. 3. Preparation, characterization, and bioevaluation of MetaCell. (A) Graph illustrating the cell viability of neutrophils exposed to increasing concentrations of Lip@Fe-Cu-MOFs. (B) Wright-Giemsa stained optical microscopy visuals of neutrophils (NEs) and MetaCell. Scale bar, 20 μm . (C) Comparative assessment of the movement of NEs and MetaCell with and without the chemoattractant fMLP (1 nM). (D) Graph detailing the time-dependent internalization of Lip@Fe-Cu-MOFs by neutrophils. (E) Confocal microscopy visuals showing MetaCell post incubation with Lip@Fe-Cu-MOFs, highlighting nuclei with 4',6'-diamidino-2-phenylindole (DAPI) staining (Ex/Em = 350/460 nm) and Lip@Fe-Cu-MOFs with C6 labeling (Ex/Em = 465/502 nm). Scale bar, 10 μm . (F) Quantitative analysis of extracellular and intracellular iron (Fe) content in MetaCell, both in the absence and presence of PMA (10 nM). (G) Confocal microscopy images depicting 4T1 cells after 4-hour coculture with either C6-labeled Lip@Fe-Cu-MOFs or MetaCell in the presence of PMA, stained with DAPI (Ex/Em = 350/460 nm for nuclei) and C6 (Ex/Em = 465/502 nm for Lip@Fe-Cu-MOFs). Scale bar, 50 μm . (H) Time-dependent fluorescence intensity in 4T1 cells post-incorporation of C6-labeled Lip@Fe-Cu-MOFs or MetaCell in the presence of PMA. (I to K) Sequential confocal images demonstrating the escape of Lip@Fe-Cu-MOFs from endosomes in 4T1 cells postcoincubation with MetaCell in the presence of PMA for 4 hours, with subsequent NIR stimulation (1.5 W/cm², 808 nm) for 5 min. After an additional 6-hour incubation, cells were marked with LysoTracker Red and Hoechst 33342. Fluorescent signals for Hoechst 33342 (Ex/Em = 346/460 nm), FITC (Ex/Em = 488/525 nm), and LysoTracker Red (Ex/Em = 577/590 nm) were captured via confocal laser scanning microscopy (CLSM). Scale bar, 50 μm . Data are depicted as mean \pm SD ($n = 3$).

neutrophils in tandem with the targeted action of PTT, this approach positions MetaCell as a promising and efficient solution in the realm of cancer therapy.

We then conducted a comprehensive investigation into the tumor-targeted delivery capabilities of MetaCell, initially focusing on the inflammation-stimulated release of Lip@Fe-Cu-MOFs from MetaCell. In addition, we assessed the subsequent uptake of these Lip@Fe-Cu-MOFs by murine mammary cancer cells (4T1 cells) using a coculture technique. This approach allowed us to closely examine the interaction between MetaCell and the tumor cells, providing valuable insights into the specific targeting and therapeutic delivery mechanisms. Specifically, MetaCell was cocultured with 4T1 cells in the presence of PMA, an activator of protein kinase C known to trigger neutrophil autotoxicity through a ROS-dependent pathway. As shown in Fig. 3 (G and H), C6-labeled Lip@Fe-Cu-MOFs were taken up by the 4T1 cells and were well-dispersed in the cytoplasm. This is primarily due to the fact that inflammation induces the formation of neutrophil extracellular traps and ruptures the neutrophil cells, resulting in the release of encapsulated Lip@Fe-Cu-MOFs. These are subsequently transported into the cancer cells, confirming the inflammation-triggered drug release profiles of MetaCell. Moreover, we detected the ability of MetaCell to deliver Lip@Fe-Cu-MOFs in NIH-3T3 mouse fibroblast cells. Figures S15 and S16 show that minimal fluorescence intensity of C6 was measured in NIH-3T3 cells within 4 hours without PMA treatment. This observation implies that MetaCell's ability to respond to inflammatory signals plays a crucial role in ensuring its targeted therapeutic applications, particularly in the context of cancer treatment where such signals are prevalent.

Meanwhile, one of the challenges in using nanoparticle-based delivery systems is ensuring that the therapeutic agent is released at the right time and location to achieve maximum efficacy (55). For Lip@Fe-Cu-MOFs, a necessary step is to escape from the endosome to release therapeutic agents into the cytoplasm of cancer cells, a process that may influence its anticancer efficacy. Lip@Fe-Cu-MOFs are composed of thermosensitive liposomes, endowing them with the ability to respond to photothermal stimulation and undergo a conformational change, which can trigger endosomal escape and drug release in cytoplasm. We therefore investigated whether NIR laser treatment could induce this endosomal escape. 4T1 cells were cocultured with MetaCell containing FITC isomer-labeled Lip@Fe-Cu-MOFs for 4 hours in the presence of PMA, followed by irradiation with an 808-nm laser (1.5 W/cm^2) for 5 min. The cells were then incubated for 6 hours and stained with LysoTracker Red for endo/lysosome labeling, and the cellular distribution of FITC was identified using CLSM. It appears that FITC labeled Fe-Cu-MOFs released from MetaCell accumulated in endosomes without NIR laser stimulation (Fig. 3, I to K), suggesting that nanoparticles can enter endosomes autonomously without external stimulation. Conversely, NIR laser stimulation induced endosome disruption, leading to low colocalization of FITC and LysoTracker Red after 6 hours of incubation. In addition, we performed Pearson's correlation coefficient analysis to identify the accumulation of Lip@Fe-Cu-MOFs in endosomes. A Pearson's correlation coefficient of 0.904 suggests a strong positive correlation between FITC and LysoTracker Red, indicating that Lip@Fe-Cu-MOFs are trapped in endosomes post-endocytosis. However, NIR laser usage notably improves the endosomal escape of Fe-Cu-MOFs, demonstrated by a decrease in the correlation coefficient to 0.692.

In vitro anticancer effects of MetaCell

A critical step in the development and testing of any previously unidentified therapeutic approach like MetaCell is safety assessment, which may help ensure that an efficient therapy will not cause undue harm to healthy cells. To measure the cytotoxicity of MetaCell, commonly used in vitro assays include the MTT [3-(4,5-dimethylthiazol-2-yl)-2,5-diphenyltetrazolium bromide] assay or the calcein acetoxymethyl ester (calcein AM)-PI (propidium iodide) staining assay. These methods can provide information on cell viability and cell death. We therefore assessed the cytotoxicity of MetaCell in healthy cells by coculturing NIH-3T3 mouse embryonic fibroblast cells with MetaCell for 24 hours without NIR irradiation. Subsequently, we measured NIH-3T3 cell viability using the MTT assay. Figure S4 reveals no significant cell death after incubation with MetaCell, suggesting its safety and the absence of potential side effects. Furthermore, we evaluated the anticancer effects of MetaCell against 4T1 cancer cells. These cells were treated with MetaCell for 4 hours using a transwell method, with or without PMA, and subsequently irradiated with or without an NIR laser (808 nm, 1.5 W/cm^2) for 5 min. After a 24-hour period, we measured cell viability. As illustrated in Fig. 4A, MetaCell combined with PMA showed a potent anticancer effect under NIR irradiation, indicating its effectiveness against cancer cells. In addition, the calcein AM-PI staining assay confirms that MetaCell with PMA, when subjected to NIR irradiation, induced a comparable level of cell death to Lip@Fe-Cu-MOFs (~60%) (Fig. 4B). This suggests that the induction of synergistic cuproptosis and ferroptosis by MetaCell is a tumor-targeted anticancer treatment.

Evaluation of anticancer mechanisms of MetaCell

A comprehensive exploration of MetaCell's interaction with cuproptosis and ferroptosis could potentially illuminate the core anticancer mechanisms of MetaCell. One conceivable mechanism might be that MetaCell triggers ROS production via the catalytic breakdown of H_2O_2 , which subsequently leads to oxidative harm. To investigate this, we measured the ROS production capacity of MetaCell in 4T1 cancer cells. As depicted in Fig. 4C, Lip@Fe-Cu-MOFs, once released from MetaCell and accumulated within cancer cells, were able to induce ROS production when subjected to light irradiation. Alternatively, the ROS might be generated through Lip@Fe-Cu-MOFs released from MetaCell disrupting cellular antioxidant defense mechanisms. For instance, Lip@Fe-Cu-MOFs could potentially deplete cellular GSH, a critical antioxidant, or inhibit the action of antioxidant enzymes like catalase or superoxide dismutase. As a continuation of this line of investigation, we quantified the intracellular levels of GSH during the MetaCell treatment process. As shown in Fig. 4D, Lip@Fe-Cu-MOFs, once released from MetaCell, effectively functioned as a redox mediator and were capable of depleting GSH in cancer cells under NIR irradiation. Given the fundamental role of GSH in safeguarding cells from oxidative stress, its depletion has been associated with a heightened susceptibility to oxidative damage and, consequently, cell death.

In addition, cuproptosis, a recently discovered form of cell death, is instigated by the binding of copper to particular lipoylated components of the TCA cycle, a sequence of metabolic reactions within mitochondria (22). This binding precipitates proteotoxic stress or damage to proteins, ultimately resulting in cell death. To substantiate the anticancer function of MetaCell in triggering cuproptosis, we performed Western blotting analysis to detect key proteins

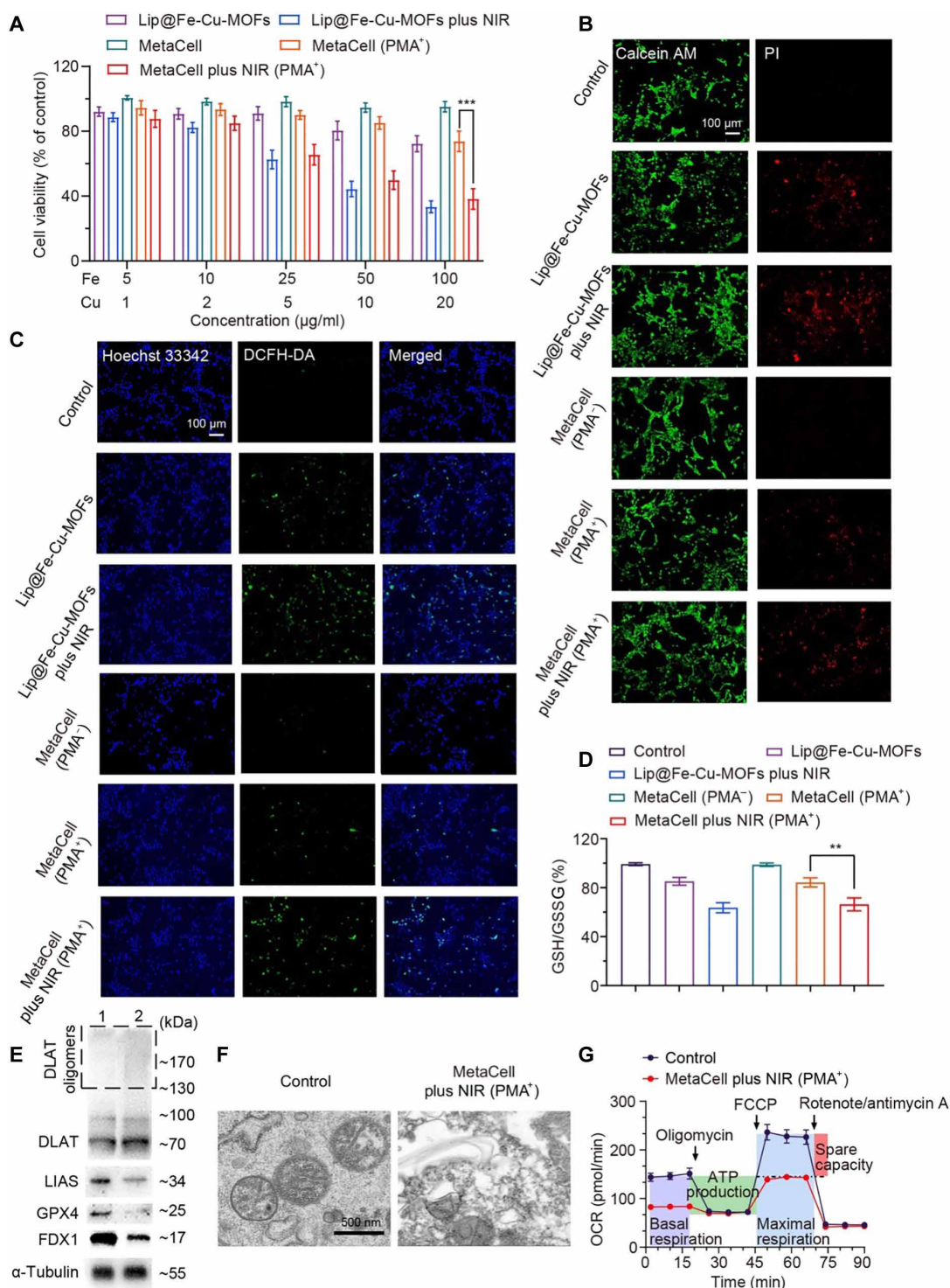


Fig. 4. In vitro anticancer effects of MetaCell on 4T1 cancer cells. (A) Anticancer effects of MetaCell on 4T1 cells. Cancer cells were coincubated with either Lip@Fe-Cu-MOFs or MetaCell with or without PMA. After a 4-hour incubation, the cells were treated with NIR and then evaluated with the MTT assay 24 hours later. (B) Live-dead staining of 4T1 cells after the treatment. 4T1 cells were coincubated with Lip@Fe-Cu-MOFs or MetaCell with or without PMA and then irradiated with NIR light. After irradiation, cells were stained with calcein AM-PI dye to visualize living and dead cells. (C) Intracellular ROS levels after the treatment. The effect of MetaCell treatment on the ROS generation was measured using the ROS dye DCFH-DA. (D) The intracellular levels of GSH in 4T1 cells after the MetaCell treatment, measured with a GSH/GSSG ratio assay kit. (E) Western blot analysis of the protein expressions of DLAT, LIAS, FDX1, and GPX4 in 4T1 cells after treatment with either neutrophils (1) or MetaCell (2) with PMA and NIR irradiation. (F) An ultrastructural analysis of MetaCell-treated 4T1 cells using TEM. (G) The oxygen consumption rate (OCR) of 4T1 cells after the treatment with either NEs or MetaCell with PMA and NIR. This provides insights into the impacts of the treatments on cellular respiration. The data in all panels are presented as mean \pm SD ($n = 3$). $**P < 0.01$ and $***P < 0.001$ (Student's t test, two tails).

implicated in this process. 4T1 cancer cells were cocultured with MetaCell plus PMA for 4 hours and then irradiated with an NIR laser (808 nm, 1.5 W/cm², 5 min). After an additional 24-hour incubation, cells were harvested, lysed, and analyzed through Western blotting. As illustrated in Fig. 4E, MetaCell promoted the oligomerization of lipoylated DLAT, a component of the pyruvate dehydrogenase complex. Its lipoylated form is vulnerable to oxidative damage. The accumulation of lipoylated proteins signifies increased oxidative stress, a characteristic trait of cuproptosis, bolstering the theory that MetaCell induces cuproptosis. Moreover, the involvement of Fe-S cluster proteins ferredoxin 1 (FDX1) and lipoyl synthase (LIAS)-mediated DLAT aggregation in cuproptosis underscores the far-reaching effects of disrupted metal homeostasis on cellular processes. Notably, the accumulation of Cu can disrupt the Fe-S cluster proteins, leading to FDX1 and LIAS inactivation, which subsequently affects their downstream targets. We hence assessed the expression of FDX1 and LIAS in MetaCell-treated cancer cells. As shown in Fig. 4E, treatment with MetaCell plus NIR laser irradiation resulted in a substantial decrease in FDX1 and LIAS levels compared to the control. This suggests that MetaCell may induce cell death through the initiation of cuproptosis and subsequent disruption of iron-sulfur cluster biogenesis.

MetaCell has been engineered to induce both cuproptosis and ferroptosis due to its ability to manipulate intracellular levels of metal ions, particularly copper and iron. In light of this, we examined MOFs' capacity to trigger ferroptosis alongside cuproptosis. Previous research has demonstrated that GSH peroxidase 4 (GPX4) plays a crucial role in the reduction of lipid hydroperoxides and that inhibition of GPX4 activity can indeed instigate ferroptosis-associated cell death. The loss of GPX4 functionality leads to an accumulation of lipid peroxides and subsequent membrane damage, culminating in ferroptosis (56). Thus, GPX4 is considered a notable biomarker and a potential therapeutic target for ferroptosis. Therefore, we evaluated the expression of ferroptosis-related proteins, such as GPX4. Figure 4E reveals that a combined treatment of MetaCell and NIR laser irradiation resulted in more pronounced down-regulation of GPX4 in cancer cells compared to other treatment groups. This highlights the role of MetaCell in the induction of both cuproptosis and ferroptosis, thereby offering the potential to target multiple cancer cell vulnerabilities simultaneously. To further elucidate the anticancer mechanism *in vitro*, we evaluated the gene expression in 4T1 cancer cells following MetaCell treatment. As depicted in Fig. S8, the combination of MetaCell and NIR laser irradiation affected the expression of genes associated with cuproptosis and ferroptosis in 4T1 cancer cells, including DLAT, LIAS, FDX1, and GPX4. This resulted in a significant up-regulation of DLAT and a down-regulation of LIAS, FDX1, and GPX4, which are consistent with those from the Western blotting assay. Furthermore, it has been established that ferroptosis typically inflicts severe damage to mitochondria, resulting in changes to mitochondrial size and membrane density (57). We then examined mitochondrial changes post-MetaCell treatment. TEM images in Fig. 4F display normal mitochondrial morphology in the control group. In contrast, tumor cells in the MetaCell-treated group exposed to laser stimulation exhibited typical characteristics of ferroptosis, indicating that MetaCell-mediated combined treatment can effectively induce ferroptosis.

Furthermore, mitochondria indeed serve crucial roles in regulating a variety of metabolic activities that are fundamental for cellular function and survival, including adenosine triphosphate (ATP)

synthesis, ROS generation, and cell apoptosis (58). Specifically, cancer cells are able to adapt to harsh microenvironments due to their capacity for metabolic reprogramming. Cancer cells often exhibit altered metabolism, which includes a shift toward glycolysis even in the presence of oxygen (a phenomenon known as the Warburg effect), which can help them survive in hypoxic environments. Furthermore, cancer cells may display altered expression of genes involved in stress response pathways, which can help them withstand oxidative conditions (59). Given that mitochondria play integral roles in both energy metabolism and programmed cell death, we examined cellular respiration behaviors during treatment. We cotreated 4T1 cells with MetaCell and NIR laser stimulation and then evaluated mitochondrial function in the cells. Initially, cells were sequentially treated with mitochondrial respiration inhibitors, such as oligomycin, carbonyl cyanide *p*-trifluoromethoxyphenylhydrazone (FCCP), and a combination of antimycin A and rotenone. This allowed us to measure ATP production, mitochondrial membrane potential, and basal respiration using a Seahorse-XF24. Figure 4G and Fig. S5 reveal that MetaCell treatment in conjunction with NIR laser stimulation resulted in a decrease in mitochondrial respiratory function. Notably, the treated group displayed lower levels of both basal respiration and maximal respiration compared to the control group. This suggests that the MetaCell treatment, in combination with NIR laser stimulation, can effectively suppress mitochondrial respiratory function. In addition, we observed a decrease in the respiratory spare capacity following MetaCell treatment. This implies that the treatment may disrupt the ability of cells to cope with stress by reducing the amount of available oxygen to cancer cells. On the basis of the current data, it appears that the application of MetaCell can enhance the efficacy of combined anticancer treatments.

In vivo tumor targeting of MetaCell

The efficacy of cancer treatments hinges upon the accumulation and penetration of therapeutics within tumors, since treatment success depends on a drug's ability to target and destroy cancer cells while minimizing harm to healthy tissues. Unfortunately, a lack of specificity in many traditional cancer therapies often leads to detrimental effects on normal tissues, which undermines the potential for successful treatment (60). In this study, we designed MetaCell using live neutrophils, an approach grounded in the understanding that neutrophil-based drug delivery systems offer a compelling means for targeted cancer therapy. This stems from neutrophils' unique ability to actively home in on inflammatory sites, including tumors (61). For drug delivery, neutrophils can skillfully evade clearance mechanisms and permeate biological barriers, thereby amplifying the delivery of therapeutic cargo to the tumor site. However, using neutrophils as drug carriers comes with inherent drawbacks, such as their naturally short lifespan, potential to elicit immune responses, and the variability in their performance depending on the individual's health status. These factors can potentially limit the effectiveness and predictability of neutrophil-mediated drug delivery (62, 63). To overcome these challenges, advanced engineering techniques can be used to extend the functions of neutrophils and enhance their targeting accuracy (64, 65). In addition, incorporating fluorescent dyes within these cells can provide real-time feedback on their location and status, enabling more precise and controlled drug delivery. By addressing these inherent limitations, the therapeutic potential of neutrophils as drug carriers can be improved.

Our MetaCell system in combination of mild photothermal effect can induce an inflammatory response, potentially boosting inflammation levels within tumors and thus augmenting MetaCell recruitment to the tumors. We therefore proceeded to explore whether MetaCell's photothermal effect could amplify self-recruitment to tumor sites after multiple treatments (Fig. 5A). We initially evaluated the tumor-targeting capability of 1,1-dioctadecyl-3,3,3-tetramethylindotricarbocyanine iodide (DiR)-labeled MetaCell (MetaCell_{DiR}) in a 4T1 orthotopic breast tumor mouse model, using DiR-labeled Lip@Fe-Cu-MOFs (Lip@Fe-Cu-MOFs_{DiR}) and blank DiR-labeled neutrophils (NEs_{DiR}) as controls. The tumor-bearing mice were intravenously administered with Lip@Fe-Cu-MOFs_{DiR}, NEs_{DiR}, or MetaCell_{DiR} every 2 days, followed by NIR laser irradiation (808 nm, 1.5 W/cm², 5 min) 24 hours post-administration. Fluorescent signals in tumor regions were monitored for 7 days (Fig. 5B). Figure 5C and figs. S9 to S11 demonstrate comparable tumor region accumulation of NEs_{DiR} and Lip@Fe-Cu-MOFs_{DiR} across four administrations. However, MetaCell_{DiR} exhibited superior tumor-targeting ability after multiple administrations and irradiations, achieving 1.65-fold and 1.55-fold higher fluorescence intensity than NEs_{DiR} and Lip@Fe-Cu-MOFs_{DiR}, respectively. Ex vivo tumor distribution data further confirmed that, after four-cycle administration, a greater concentration of MetaCell was present in tumor tissues in comparison to NEs_{DiR} and Lip@Fe-Cu-MOFs_{DiR} (Fig. 5, D and E, and figs. S9 and S10). Concurrently, fig. S6 indicates that NIR-irradiated MetaCell can intensify intratumor inflammation, significantly elevating the levels of tumor necrosis factor- α (TNF- α), interleukin-6 (IL-6), and IL-10. The obviously stronger DiR fluorescent signal evident in 7-day treated tumor tissues, as compared to those treated with Lip@Fe-Cu-MOFs (Fig. 5F), suggests that the MetaCell-mediated mild photothermal effect can increase tumor inflammation, which in turn attracts more MetaCell to the tumors, culminating in high tumor accumulation.

Neutrophils, integral to the body's innate immune response, typically have a brief lifespan ranging from approximately 0.75 to a couple of days. This transient nature presents substantial challenges for their deployment as drug carriers, particularly in treatments requiring extended or controlled drug release. Once activated, neutrophils quickly undergo apoptosis (programmed cell death) and are eliminated from the body, notably narrowing the available timeframe for effective drug delivery (63). Moreover, variables like an individual's health condition, infection presence, or systemic inflammation can further reduce their lifespan, complicating the predictability and management of drug delivery duration (66). The rapid turnover of neutrophils raises concerns about the premature release of encapsulated drugs before reaching the intended target, potentially diminishing treatment efficacy and escalating side effects. To counter these challenges, innovative strategies, such as mechanisms for targeted drug release at the site of action, are crucial to use the limited lifespan of neutrophils effectively.

To surmount these challenges, we have innovated MetaCell, incorporating a self-amplifying tumor-targeting mechanism. Harnessing the natural properties of neutrophils, MetaCell adeptly evades immune surveillance and effectively infiltrates tumor tissues, releasing therapeutic agents in response to inflammatory cues. Critically, MetaCell is expertly engineered to amplify tumor inflammation through photothermal effects, thereby facilitating its enhanced accumulation at tumor sites. To verify the stability of MetaCell during deployment, we used a dual-labeling technique

[3,3-Dioctadecyloxycarbocyanine (DiO) to label neutrophils and DiR for Lip@Fe-Cu-MOFs], ensuring the integrity of MetaCell throughout the delivery process. In our study, mice with tumors received these dual-labeled MetaCells via bidaily intravenous injections, followed by NIR laser exposure (808 nm, 1.5 W/cm²) after 24 hours. After a 7-day treatment period, there was a marked increase in both DiO and DiR fluorescence in the tumors, as illustrated in fig. S17, confirming that MetaCells not only effectively targeted but also remained structurally intact within the tumor environment. Furthermore, Fig. 5G underscores the potent photothermal response of MetaCell, with the tumor site temperature escalating to 48.6°C within 5 min of laser stimulation. This photothermal characteristic is crucial in cancer therapy, as it ensures the direct and targeted delivery of therapeutic agents into tumor cells, potentially boosting treatment efficacy while minimizing adverse effects on healthy tissues. The successful implementation of MetaCell, overcoming the inherent limitations of neutrophils, substantially expands their potential in drug delivery applications, thereby enhancing their practicality and effectiveness for therapeutic interventions.

In vivo antitumor effects of MetaCell

In vivo antitumor effects represent the capacity of a substance or treatment to inhibit or reduce tumor growth within a living organism. These effects are often examined in orthotopic tumor-bearing mice models, facilitating the evaluation of tumor growth and treatment response in a microenvironment closely simulating human disease conditions. Consequently, we evaluated the antitumor effects of MetaCell in a 4T1 orthotopic tumor-bearing mice model. Mice were intravenously administered with phosphate-buffered saline (PBS), Lip@Fe-Cu-MOFs (10 mg/kg of Fe), or MetaCell (2×10^7 cells per mouse), followed by exposure to NIR laser irradiation (808 nm, 1.5 W/cm²) for 5 min, 24 hours postinjection. This anticancer treatment was performed every other day for a total of eight treatments, while tumor growth was monitored over a 16-day period (Fig. 6A). The control group was composed of MetaCell-treated mice without laser irradiation. As illustrated in Fig. 6 (B and C), the combined therapy of MetaCell and NIR laser irradiation demonstrated effective tumor ablation after 16 days of treatment, indicating its potent antitumor efficacy. Notably, MetaCell exhibited superior antitumor effects compared to Lip@Fe-Cu-MOFs, implying that neutrophil modifications enhance antitumor efficacy. This outcome likely results from MetaCell's ability to specifically target cancer cells, with NIR laser activation triggering a direct drug release into the tumor. No significant changes in mouse body weights were observed throughout the 16-day treatment (Fig. 6D), suggesting excellent biosafety of MetaCell. In addition, hematoxylin and eosin (H&E) staining of tumor tissues was conducted to discern the antitumor effects within each group. H&E staining, within the context of tumor tissues, provides the information on histological subtypes, as well as the presence of necrosis and other pathological features. Figure 6E reveals obvious tumor cell remission, signified by the reduction in tumor cell size or number following treatment. Specifically, the combined treatment of MetaCell and NIR laser irradiation resulted in a higher level of necrosis compared to other groups. These data suggest that the utilization of MetaCell can be effective in inhibiting tumor growth and potentially reducing tumor size.

It is crucial to highlight that further investigation into the antitumor mechanism of MetaCell is needed. Our first assessment focused on GSH levels within tumor tissues. As displayed in Fig. 6F, the

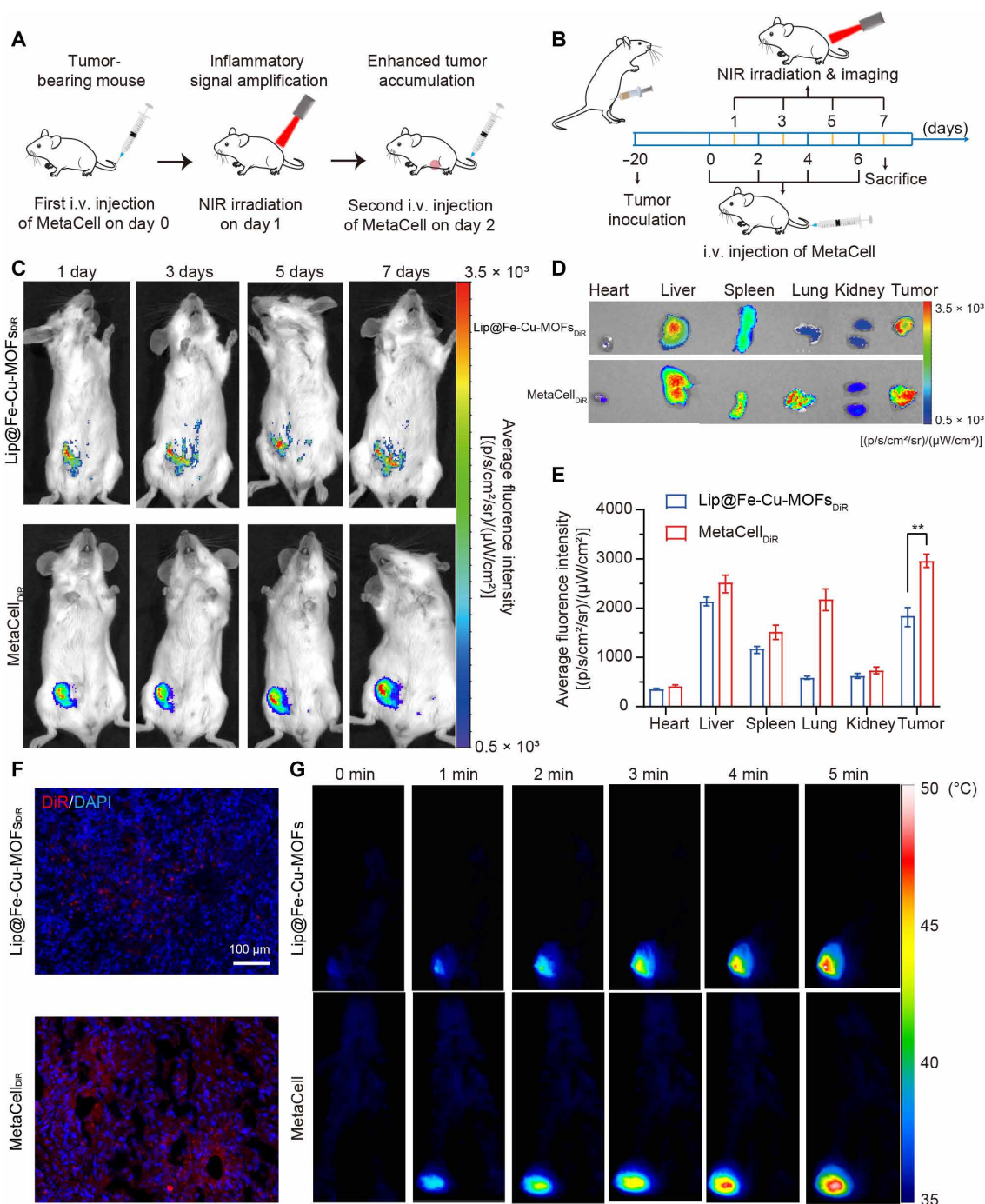


Fig. 5. Enhanced tumor targeting of MetaCell in vivo. (A) Schematic of inflammation-induced amplified recruitment of MetaCell to tumors, facilitated by a mild photo-thermal effect. (B) Therapeutic protocol detailing MetaCell administration. Mice bearing tumors were intravenously (i.v.) injected with Lip@Fe-Cu-MOFs_{DiR} [Fe (10 mg/kg)] or MetaCell_{DiR} (2×10^7 cells per mouse) every 2 days for 4 cycles, followed by a 5-min NIR laser stimulation (808 nm, 1.5 W/cm^2). The accumulation of Lip@Fe-Cu-MOFs_{DiR} and MetaCell_{DiR} was monitored over 7 days with an In Vivo Imaging System. In the imaging protocol for DiR, a filter set with a 710-nm excitation wavelength and a 760-nm emission wavelength was used. The images were captured with an exposure time of 10 s, using an extended NIR range 150-W Tungsten EKE light source. (C) Time-dependent analysis of MetaCell targeting in mice bearing 4T1 tumors over a course of 7 days. (D and E) The biodistribution of Lip@Fe-Cu-MOFs_{DiR} or MetaCell_{DiR} in tumor sites and major organs, 7 days post-administration. In the imaging protocol for DiR, a filter set with a 710-nm excitation wavelength and a 760-nm emission wavelength was used. The images were captured with an exposure time of 10 s, using an extended NIR range 150-W Tungsten EKE light source. (F) Ex vivo tumor distribution of Lip@Fe-Cu-MOFs_{DiR} or MetaCell_{DiR} in tumor tissues, 7 days post-administration. Scale bar, 100 μm. (G) MetaCell-mediated photothermal imaging of 4T1 tumor-bearing mice. Mice were intravenously injected with Lip@Fe-Cu-MOFs [Fe (10 mg/kg)] or MetaCell (2×10^7 cells per mouse), followed by a 5-min laser irradiation (808 nm, 1.5 W/cm^2), 24 hours post-administration. Subsequently, tumor tissue was imaged using a thermal imaging camera. The data are presented as mean \pm SD ($n = 5$), $**P < 0.01$ (Student's *t* test, two tails).

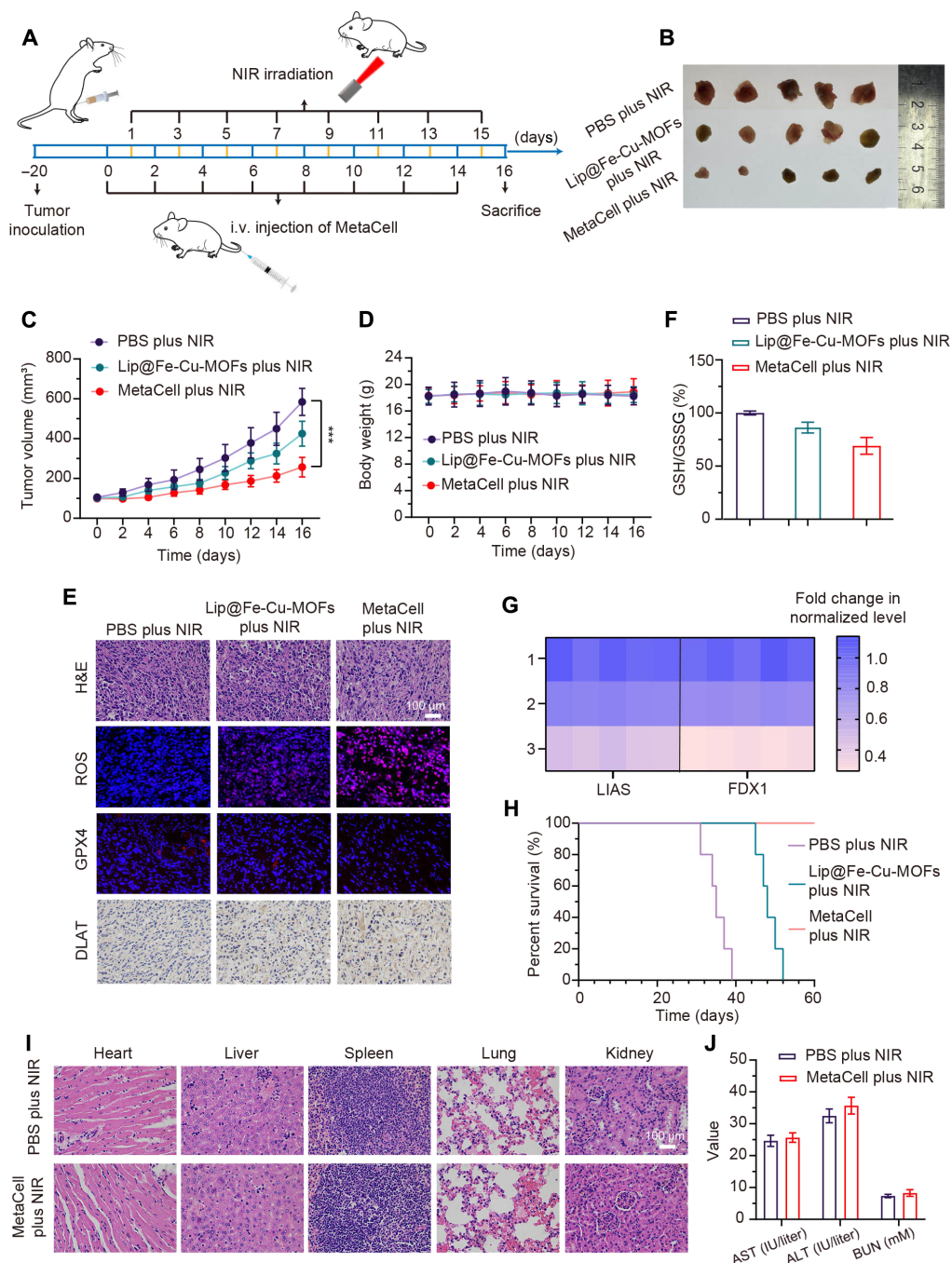


Fig. 6. Evaluation of in vivo antitumor capabilities of MetaCell. (A) Therapeutic protocol illustrating MetaCell administration. (B) Visualization of tumor specimens following treatment. Mice were treated intravenously with PBS, Lip@Fe-Cu-MOFs [Fe (5 mg/kg)], or MetaCell (2×10^7 cells per mouse) every 2 days, with a total of eight rounds of administration, followed by NIR stimulation (1.5 W/cm^2 , 808 nm) for 5 min, administered 24 hours postinjection. After the 16-day treatment, mice were euthanized, and tumors were subsequently harvested and imaged. (C) Tumor growth trajectories in 4T1 tumor-bearing mice post-MetaCell treatment. Tumor progression was monitored over a 16-day period. (D) Body weight fluctuations of 4T1 tumor-bearing mice over the 16-day treatment span. (E) Representative images of tumor sections stained with H&E, ROS, GPX4, and DLAT posttreatment. Mice were euthanized following the 16-day treatment period, and tumors were harvested, sectioned, and stained with H&E, ROS, GPX4, and DLAT. Scale bar, 100 μm . (F) Assessment of GSH depletion in tumor tissues: After a 16-day treatment regimen, euthanized mice's tumors were excised, homogenized, and subjected to centrifugation. The GSH levels in the resultant supernatant were measured using a GSH and GSSG assay kit. (G) Capability of MetaCell to suppress FDX1 and LIAS expression. After 16-day treatment, 4T1 tumor-bearing mice from each group were euthanized, and tumors were harvested, homogenized, and centrifuged for subsequent LIAS and FDX1 expression assessment via quantitative real-time PCR (qRT-PCR). (H) Survival tracking of tumor-bearing mice over the course of the 60-day treatment in each group. (I) Histopathological evaluation via H&E staining of critical organ tissues after 16-day MetaCell plus NIR treatment. Scale bar, 100 μm . (J) Concentrations of ALT, AST, and BUN in mouse serum after 16-day MetaCell plus NIR treatment period. Data are represented as mean \pm SD, ($n = 5$). *** $P < 0.001$ [one-way analysis of variance (ANOVA)].

combined treatment of MetaCell and NIR laser notably affected intratumor GSH levels. Specifically, GSH levels significantly decreased in the group subjected to the combined therapy compared to other groups. This decrease suggests that synergistic ferroptosis and cuproptosis could effectively induce tumor cell death. Furthermore, this synergistic effect was anticipated to enhance ROS generation in tumor tissue upon stimulation, leading to tumor destruction. We measured ROS levels in tumor tissues using dihydroethidium (DHE) staining. DHE, a cell-permeable compound, is oxidized by ROS to form a fluorescent product called ethidium, detectable by fluorescence microscopy. Figure 6E demonstrates that the combined treatment of MetaCell and NIR laser irradiation substantially elevated ROS levels in tumor tissues. This is because the buildup of ferroptosis-mediated lipid peroxides and copper ions can contribute to ROS production, which in turn leads to cell death. We further evaluated DLAT and GPX4 levels in MetaCell-treated tumor tissues using a Western blotting assay. As shown in Fig. 6E, DLAT levels increased in the treatment group, while GPX4 levels decreased, suggesting that the treatment exerted its antitumor effect through a process called the cuproptosis-ferroptosis synergistic effect. We also assessed the FDX1 and LIAS levels in MetaCell-treated tumor tissues through real-time polymerase chain reaction (PCR). As displayed in Fig. 6G, the LIAS and FDX1 levels in the MetaCell plus NIR group were significantly lower compared to the PBS group, underscoring the antitumor effects of cuproptosis.

Notably, as illustrated in Fig. 6H, MetaCell therapy produced a 100% survival rate across a 60-day observation period. Conversely, the median survival durations in the PBS control group and the Lip@Fe-Cu-MOFs group were a mere 35 days and 48 days, respectively, emphatically highlighting the superior therapeutic advantages of MetaCell treatment. We further assessed the biocompatibility of MetaCell by scrutinizing key organs, encompassing the heart, liver, spleen, lungs, and kidneys. After treatment, these organs were harvested and subjected to H&E staining for histological evaluation. As depicted in Fig. 6I, MetaCell treatment did not result in discernible pathological damage, cellular disruption, or inflammation when compared with the PBS group. Figure 6J reveals that MetaCell therapy did not induce significant alterations in the concentrations of aspartate aminotransferase (AST) and alanine aminotransferase (ALT), which serve as indices of liver function, or blood urea nitrogen (BUN), a renal function indicator, in comparison to the control group administered with PBS. These data suggest that the coactivation of cuproptosis and ferroptosis within a therapeutic context can potentially augment the efficacy of conventional cancer interventions. The concurrent triggering of these distinct modes of regulated cell death may present a potent approach for eradicating cancer cells while preserving high biocompatibility, considering that each process targets discrete facets of cellular metabolism and metal ion homeostasis.

DISCUSSION

In summary, our study notably enhances the understanding of metal homeostasis in cancer therapy, particularly emphasizing the roles of copper and iron. The MetaCell system, an innovative integration of cuproptosis and ferroptosis, leverages Fe^{3+} and Cu^{2+} in Fe-Cu-MOFs to catalyze Fenton/Fenton-like reactions, producing hydroxyl radicals that, in conjunction with Cu^{2+} , effectively deplete GSH in tumor cells. This approach innovatively unites two distinct pathways

of regulated cell death, highlighting the effectiveness of our method. Using live neutrophils as carriers for thermosensitive liposomal Fe-Cu-MOFs, the MetaCell system demonstrates substantial efficacy against cancer cells, both in vitro and in vivo. Furthermore, MetaCell's ability to mimic neutrophil properties enables it to effectively evade the immune system, penetrate tumors, and maintain stability under various conditions. This innovative approach not only shows notably promise in treating solid tumors and reducing cancer recurrence but also extends survival in tumor-bearing mice. The safety profile of the MetaCell system, evidenced by the absence of adverse effects on major organ functions, suggests its potential for clinical translation.

Despite its promising results, the MetaCell system does face potential limitations and areas for future research. One such limitation is the need for precise control over the activation and release of the therapeutic payload, ensuring targeted delivery while minimizing potential off-target effects. In addition, the inherent short lifespan of neutrophils presents challenges in sustaining the delivery of therapeutic agents, necessitating further exploration into extending their functional duration or developing alternative delivery strategies. Future research should also focus on the scalability and reproducibility of the MetaCell system for clinical applications, as well as its adaptability to various cancer types and potentially other diseases. Moreover, exploring the interactions of MetaCells with different tumor microenvironments and the immune system will be crucial in optimizing their efficacy and safety. By addressing these challenges and extending the scope of research, the MetaCell system could potentially revolutionize the landscape of cancer therapy and beyond.

MATERIALS AND METHODS

Materials

All used chemicals and solvents are of reagent grade unless explicitly stated otherwise. Sigma-Aldrich (St. Missouri, USA) and Aladdin Reagent Co. Ltd. (Shanghai, China) supplied the chemicals used in the study, all of which are used without additional purification. Soybean PC, cholesterol, and DPPC are sourced from AVT (Shanghai) Pharmaceutical Tech Co. Ltd. (Shanghai, China). DSPE-PEG2000 is procured from ToYongBio Tech Co. Ltd. (Shanghai, China). Various reagents and solutions, including Wright-Giemsa staining solution, Crystal Violet staining solution, Dulbecco's modified Eagle's medium (DMEM), trypsin-EDTA (0.25%), and tris-buffered saline with Tween 20, are purchased from Jiangsu KeyGEN BioTECH Co. Ltd. (Nanjing, China). Fetal bovine serum (FBS) is procured from Sijiqing (Hangzhou, China). Further, Hoechst 33342, LysoTracker Red, 2'-7'-dichlorofluorescein diacetate (DCFH-DA), radioimmunoprecipitation (RIPA) lysis buffer, 4',6-diamidino-2-phenylindole (DAPI), and GSH and GSSG assay kits, along with live and dead viability/cytotoxicity assay kits, are supplied by Beyotime Institute of Biotechnology Co. LLC. (Nantong, China). Antibodies, such as rabbit anti- α -tubulin, goat anti-rabbit immunoglobulin G (H + L), and DiR are also procured from the same supplier. TRIzol reagent is sourced from Invitrogen (California, USA). Alexa Fluor 488 anti-CD11b antibody (catalog no. ab307387) was purchased from Abcam (Cambridge, UK). DLAT polyclonal antibody, GPX4 polyclonal antibody, LIAS polyclonal antibody, and FDX1 polyclonal antibody are purchased from Proteintech (Rosemont, USA). Enzyme-linked immunosorbent assay (ELISA) kits of TNF- α (catalog no. DY410-05), IL-6 (catalog no. DY406-05), and IL-10 (catalog no. DY417-05) are

purchased from the R&D System (Minneapolis, USA). Last, the cDNA RT Kit is obtained from TaKaRa Biotechnology Co. Ltd. (Dalian, China).

Cell lines and animals

The NIH-3T3 and 4T1 cell lines used in this research are procured from the Cell Bank of Chinese Academy of Science (Shanghai, China). These cell lines are cultured in DMEM enriched with 10% FBS (v/v) and 1% penicillin/streptomycin (w/v). The cell cultures are maintained at 37°C within a humidified atmosphere of 5% CO₂, facilitated by a CO₂ incubator (Forma Series 2 Water Jacket 3111, Thermo Fisher Scientific, USA). BALB/c mice, aged 7 weeks and weighing between 18 and 22 g, are sourced from Skbex Biotechnology (Henan, China). All animal-based experiments are conducted in compliance with the National Institute of Health Guidelines and under the protocols that are approved by the Ethics Committee at the Affiliated Drum Tower Hospital of Nanjing University Medical School [SYXK(Su)2019-0056].

Synthesis and characterization of Fe-Cu-MOFs

Fe-Cu-MOFs were synthesized using a slightly modified solvothermal method (67). Initially, FeCl₃·6H₂O (1.62 g), CuCl₂·2H₂O (0.68 g), and 1,4-benzendicarboxylic acid (1.50 g) were thoroughly dissolved in 70 ml of DMF. This mixture was subsequently maintained at 100°C for 12 hours. The resultant precipitate was then rinsed with water via centrifugation before being lyophilized, yielding a product denoted as Fe-Cu-MOFs. The particle size and zeta potential of the Fe-Cu-MOFs were assessed using a DLS (Zetasizer Nano ZS90, Malvern, UK) technique, while their morphology was inspected through TEM (JEM-1400, JEOL, Japan). XRD patterns were procured using an x-ray diffractometer (D8 Discover, Bruker, Germany) across the scanning range of 10° to 90°. The specific Fe or Cu content within the Fe-Cu-MOFs was established by using SEM-EDS and ICP-MS (NexION 300x, PerkinElmer, USA).

Synthesis and characterization of Lip@Fe-Cu-MOFs

Lip@Fe-Cu-MOFs were prepared using a film dispersion method. Briefly, a blend of 50 mg of PC, 50 mg of DPPC, 25 mg of cholesterol, and 10 mg of DSPE-PEG2000 was adequately dissolved in a 20-ml mixture of ethanol and dichloromethane (4:1, v/v). The resultant solution was evaporated under a 40°C temperature in a round-bottom flask to form a thin lipid film. This film was then hydrated using 10 ml of Fe-Cu-MOFs (6 mg/ml) at 50°C for 30 min. The formed suspension was ultrasonicated for 20 min at 300 W in an ice-water bath using an ultrasonic cell crusher (XO-650D, Xianou Industrial Co. Ltd., China), following a cycle of 1-s ultrasonication and 2-s intervals. The liposome suspension was further purified using a 0.22-μm cellulose nitrate membrane to discard any precipitated Fe-Cu-MOFs, resulting in Lip@Fe-Cu-MOFs. The Fe or Cu content within Lip@Fe-Cu-MOFs was established via SEM-EDS, XPS and ICP-MS measurements. For the control formulation, Lip@Fe-Cu-MOFs_{C6} or Lip@Fe-Cu-MOFs_{DiR} were prepared by adding 10 mg of C6 or 500 μg of DiR into the round-bottom flask during the lipid film formation stage. Concurrently, Lip@Fe-Cu-MOFs_{FITC} was created by labeling Fe-Cu-MOFs with FITC. The particle size, zeta potential, and morphology of Lip@Fe-Cu-MOFs were gauged through DLS and TEM. To assess size stability, Lip@Fe-Cu-MOFs were suspended in equivalent volumes of PBS, DMEM, and FBS separately, and the particle sizes post a 48-hour incubation at 37°C were measured using DLS.

Photothermal-responded release of Lip@Fe-Cu-MOFs

Lip@Fe-Cu-MOFs, with an Fe concentration of 120 μg/ml, were exposed to an 808-nm laser (1.5 W/cm²) for 5 min, both with and without irradiation, and the resulting temperature change curves were documented using a temperature detector (AT4204, Applent, China). To explore the photothermal-responsive release of Lip@Fe-Cu-MOFs, a solution of Lip@Fe-Cu-MOFs_{C6} was enclosed in a dialysis bag (molecular weight cut off: 1000 Da) and immersed in 50 ml of PBS. After incubating for half an hour, the sample was stimulated by an 808-nm laser (1.5 W/cm²) for 5 min. The concentrations of C6 [excitation/emission (Ex/Em) = 465/502 nm] in the dialysate at various time points (0, 0.25, 0.5, 1, 1.5, 2, 4, 8, 12, and 24 hours) were measured using a microplate reader (Infinite 200 Pro, Tecan, Switzerland). As a control, Lip@Fe-Cu-MOFs_{C6} without laser stimulation were kept in PBS.

GSH depletion of Lip@Fe-Cu-MOFs

To evaluate the GSH depletion capabilities of Lip@Fe-Cu-MOFs, samples of Lip@Fe-Cu-MOFs with various concentrations of Fe-Cu-MOFs (0, 75, 150, 300, 600, and 1200 μg/ml) were irradiated by an 808-nm laser (1.5 W/cm²) for 5 min, followed by treatment of GSH (10 mM) for 12 hours at 37°C. The samples were then treated with DTNB (2.5 mg/ml) and incubated for 5 min at 37°C. Absorbance at 412 nm of the resulting system was detected using the microplate reader. For control purposes, Lip@Fe-Cu-MOFs were used without the application of laser irradiation.

Cu⁺ generation mediated by Lip@Fe-Cu-MOFs

For assessing the generation of Cu⁺, Lip@Fe-Cu-MOFs were irradiated with an 808-nm laser (1.5 W/cm², 5 min) and then incubated with GSH at varying concentrations (0, 2.5, 5, 10, and 20 mM) for 12 hours at 37°C. Following this, the emission fluorescence intensity at 610 nm (with an excitation wavelength of 365 nm) was measured using a microplate reader. Lip@Fe-Cu-MOFs that had not been irradiated with the laser were used as the control.

Fenton/Fenton-like reaction catalyzed by Lip@Fe-Cu-MOFs

To examine the Fenton/Fenton-like reaction catalytic efficiency of Lip@Fe-Cu-MOFs, the Lip@Fe-Cu-MOFs suspension [containing Fe-Cu-MOFs (1500 μg/ml)] was mixed with an equal volume of MB (30 μg/ml) and 3 mM H₂O₂, followed by irradiation with an 808-nm laser for 5 min (1.5 W/cm²). After a 12-hour incubation period, the absorbance of MB at 660 nm was measured using a microplate reader. As a control, Lip@Fe-Cu-MOFs that did not have H₂O₂ added and were not exposed to laser irradiation were used.

Preparation and characterization of MetaCell

Mature murine neutrophils were isolated from the bone marrow of femurs and tibias of female BALB/c mice, following a previously established method (68). Approximately 1×10^7 of neutrophils were then incubated with Lip@Fe-Cu-MOFs [containing Fe-Cu-MOFs (3 mg/ml)] at 37°C for 2 hours, forming MetaCell. Following the cellular uptake process, cells were washed thrice with cold PBS and then collected through centrifugation for the subsequent use. The cell viability of MetaCell was assessed using an MTT assay. To study the cellular uptake behavior, we used Lip@Fe-Cu-MOFs_{C6} to establish fluorescence-labeled MetaCell, the fluorescence of which (Ex/Em = 465/502 nm) was characterized using a flow cytometer

(FACSVerse, BD, USA) and a CSLM (FV3000, Olympus, Japan). Meanwhile, to investigate the storage stability of Lip@Fe-Cu-MOFs inside the MetaCell, a DiI-labeled thermosensitive liposomes encapsulating FITC-labeled Fe-Cu-MOFs was prepared, which was uptaken by neutrophils to establish double fluorescence-labeled MetaCell, and the fluorescence was characterized using a CSLM. In addition, MetaCell's appearance was also characterized through Wright-Giemsa staining and observed under a microscope. The Fe or Cu content within MetaCell was established via ICP-MS measurements.

Chemotaxis evaluation of MetaCell

To evaluate the chemotaxis associated biomarkers (CD11b) of MetaCell, neutrophils or MetaCell was treated with 0, 1, and 100 nM fMLP at 37°C for 30 min and washed with cold PBS twice, followed by staining with anti-CD11b antibody for flow cytometry analysis. Meanwhile, a transwell migration assay was performed. Neutrophils or MetaCell (2×10^4 cells per well suspended in 200 μ l of DMEM) were placed in the upper chamber of a transwell (with an 8- μ m pore size and 0.33-cm² membrane surface area; Corning Costa, USA). The lower chamber was filled with DMEM, either with or without 1 nM fMLP. Following a half-hour treatment, cells in the lower chamber were observed under an optical microscope and counted using a hemacytometer to calculate the migration ratio using the following formula

$$\text{Migration ratio (\%)} = \frac{N_{\text{low}}}{N_{\text{add}}} \times 100\% \quad (1)$$

where N_{low} represents the number of cells counted in the lower compartment, and N_{add} represents the number of cells added to the upper compartment.

In vitro release properties of Lip@Fe-Cu-MOFs

To study the in vitro release characteristics of Lip@Fe-Cu-MOFs, MetaCell (2×10^4 cells per well suspended in 200 μ l of DMEM with or without 10 nM PMA) was seeded into the upper chamber of a transwell (0.4- μ m pore size and 0.33-cm² membrane surface area; Corning Costa, USA), and the lower chamber was filled with DMEM. At various time points (0, 1, 2, 3, 4, 5, and 6 hours), the suspension from the upper/lower chamber was collected, and the concentrations of Fe or Cu were determined using ICP-MS.

Cellular uptake in 4T1 cells

4T1 cells (1×10^5 cells per well) were seeded in 24-well plates and placed into the lower chamber of a transwell (0.4- μ m pore size and 0.33-cm² membrane surface area; Corning Costa, USA) and cultured overnight at 37°C. Afterward, either MetaCell (1×10^7 cells per well suspended in 200 μ l of DMEM with 10 nM PMA) or Lip@Fe-Cu-MOFs [Fe-Cu-MOFs (500 μ g/ml)] were added into the upper chamber of the transwell. This was followed by further incubation for varying lengths of time (1, 2, 4, 6, and 8 hours). Following this treatment, the intracellular fluorescence intensity in 4T1 cells was measured using flow cytometry and visualized using a fluorescence microscope.

Cellular uptake in normal cells

NIH-3T3 cells (1×10^5 cells per well) were seeded in 24-well plates and placed into the lower chamber of a transwell (0.4- μ m pore size and 0.33-cm² membrane surface area; Corning Costa, USA) and

cultured overnight at 37°C. Afterward, MetaCell (1×10^7 cells per well suspended in 200 μ l of DMEM with/without PMA) encapsulating C6-labeled Lip@Fe-Cu-MOFs were added into the upper chamber of the transwell. This was followed by further incubation for varying lengths of time (1, 2, 4, 6, and 8 hours). Following this treatment, the intracellular fluorescence intensity in NIH-3T3 cells was measured using flow cytometry.

Cellular distribution of Lip@Fe-Cu-MOFs in tumor cells

To verify the photothermal-mediated release of Lip@Fe-Cu-MOFs in tumor cells, 4T1 cells (1×10^5 cells per well) were seeded in 24-well plates and placed into the lower chamber of a transwell (0.4- μ m pore size and 0.33-cm² membrane surface area; Corning Costa, USA). They were then cultured overnight at 37°C. Afterward, FITC-labeled MetaCell (1×10^7 cells per well suspended in 200 μ l of DMEM with 10 nM PMA) was added to the upper chamber of the transwell. This was followed by further incubation for 4 hours and then irradiation with an 808-nm laser (1.5 W/cm²) for 5 min. Following 6 hours of treatment, the 4T1 cells were stained with Lyso-Tracker Red and Hoechst 33342 and then observed using a CSLM.

In vitro anticancer effects of MetaCell

To evaluate the photothermal-triggered anticancer effect of MetaCell, 4T1 cells seeded in a 24-well plate and placed in the lower chamber of a transwell (0.4- μ m pore size and 0.33-cm² membrane surface area; Corning Costa, USA) were cultured overnight at 37°C. Following this, different densities of MetaCell (1×10^7 cells per well suspended in 200 μ l of DMEM with or without 10 nM PMA) or different concentrations of Lip@Fe-Cu-MOFs [Fe-Cu-MOFs (500 μ g/ml)] were added into the upper chamber of the transwell. This was followed by further incubation for 4 hours and irradiation with an 808-nm laser (1.5 W/cm²) for 5 min. After 24 hours of treatment, the cell viability in each group was measured using an MTT assay and calcein AM-PI live-dead cell staining. Control groups were MetaCell or Lip@Fe-Cu-MOFs groups that were not irradiated with the laser.

ROS generation mediated by MetaCell

For ROS generation, 4T1 cells were seeded in a 24-well plate and placed in the lower chamber of a transwell (0.4- μ m pore size and 0.33-cm² membrane surface area; Corning Costa, USA) and were cultured overnight at 37°C. Subsequently, MetaCell (1×10^7 cells per well suspended in 200 μ l of DMEM with or without 100 nM PMA) or Lip@Fe-Cu-MOFs [Fe-Cu-MOFs (500 μ g/ml)] were added into the upper chamber of the transwell. This was followed by further incubation for 4 hours and irradiation with an 808-nm laser (1.5 W/cm²) for 5 min. After 24 hours of treatment, the cells in each group were treated with the ROS detection agent DCFH-DA (10 nM) or a GSH and GSSG assay kit, respectively.

Anticancer mechanism induced by MetaCell

For the Western blotting assay, 4T1 cells were seeded in a 24-well plate as the lower chamber of a transwell (0.4- μ m pore size and 0.33-cm² membrane surface area; Corning Costa, USA) and cultured overnight at 37°C. Subsequently, MetaCell (1×10^7 cells per well suspended in 200 μ l of DMEM with 100 nM PMA) was added into the upper chamber of the transwell, followed by further incubation for 4 hours and irradiation with an 808-nm laser (1.5 W/cm²) for 5 min. After 24 hours of treatment, the cells were harvested to generate cell

lysates and then treated with antibodies to DLAT (1:2000), LIAS (1:1000), GPX4 (1:1000), FDX1 (1:1000), or α -tubulin (1:1000). The proteins were analyzed and detected by a chemiluminescent imaging system (5200 Multi, Tanon, China).

Total RNA from the tumor cells treated with neutrophils or MetaCell with PMA and NIR irradiation was extracted using TRIzol reagent and reverse-transcribed into cDNA using a cDNA RT Kit. Quantitative real-time PCR (qRT-PCR) was performed on a StepOnePlus Real-Time PCR system (Thermo Fisher Scientific, USA). The PCR cycling conditions included an initial denaturation step at 95°C for 10 min, followed by 45 cycles of denaturation at 95°C for 15 s, and annealing/extension at 60°C for 1 min. Relative gene expression was calculated using the $2^{-\Delta\Delta C_t}$ method, with the α -tubulin gene serving as the housekeeping gene for normalization.

The primer sequences used for the qRT-PCR are as follows: DLAT: CTGAGTGAAGGAGACTTGCTGG (reverse) and TCCCAGAGGAACATCCCTTGTG (forward); LIAS: AAGATGACCTAACCAATGGACC (reverse) and AGTTGATAGAGATGATTTACCTGATG (forward); FDX1: TTCAACCTGTCACCTCATCTTTG (forward) and TGCCAGATCGAGCATGTCATT (reverse); GPX4: TGTGCATCCCGCGATGATT (forward) and CCCTGTACTTATCCAGGCAGA (reverse); α -tubulin: TC-GATATTGAGCGTCCAACCT (forward) and CAAAGGCACGTTTGGCATAACA (reverse).

The 4T1 tumor cells treated with MetaCell were also fixed and imaged using TEM to observe the morphology of the mitochondria. 4T1 tumor cells treated with DMEM were used as a control.

Regulation of energy metabolism mediated by MetaCell

For the measurement of ATP generation and oxygen consumption rate (OCR) induced by MetaCell, 4T1 cells seeded in a 24-well plate as the lower chamber of transwell (0.4- μ m pore size and 0.33-cm² membrane surface area; Corning Costa, USA) were cultured at 37°C overnight. Subsequently, MetaCell (1×10^7 cells per well suspended in 200 μ l of DMEM with 100 nM PMA) was added into the upper chamber of transwell, followed by further incubation for 4 hours and irradiating with a 808-nm laser (1.5 W/cm²) for 5 min. After 24-hour treatment, the cells were rinsed with XF Cell Mito Stress Test Assay Medium and treated for further 1 hour at 37°C, followed by adding oligomycin (1 μ M), FCCP (1 μ M), and antimycin A/rotenone (0.5 μ M). The OCR of treated cells was measured using the Seahorse-XFe24 (Agilent, USA), and data were analyzed using Seahorse Wave.

In vivo biodistribution of MetaCell

To establish the 4T1 orthotopic tumor-bearing mouse model, 4T1 cells (1×10^6 cells suspended in 100 μ l of PBS) were engrafted into the mammary fat pad of female BALB/c mice. The tumor volume (V , mm³) was calculated using the following formula

$$V = \frac{1}{2} \times a^2 \times b \quad (2)$$

where a and b represent the width and length of the tumor tissues, respectively, measured with a vernier caliper.

Once the tumors in the mice had reached a size of approximately 100 mm³, the mice were randomly divided into two groups. Each group received an intravenous injection of DiR-labeled blank neutrophils (2×10^7 cells per mouse), DiR-labeled MetaCell (2×10^7 cells per mouse), or DiR-labeled Lip@Fe-Cu-MOFs

(administered at a dosage of 10 mg/kg of Fe), respectively. Following 24 hours postinjection, the mice from each group were subjected to a 5-min irradiation with an 808-nm NIR laser (1.5 W/cm²). This treatment was repeated every 2 days for a total of four treatments over a 7-day period. Throughout the treatment, the mice underwent in vivo imaging using an In Vivo Imaging System Spectrum (PerkinElmer, USA) at specific time intervals: days 1, 3, 5, and 7. In the imaging protocol for DiR, a filter set with a 710-nm excitation wavelength and a 760-nm emission wavelength was used. The images were captured with an exposure time of 10 s, using an extended NIR range 150-W Tungsten EKE light source. On day 7 posttreatment, the tumors and major organs (heart, liver, spleen, lungs, and kidneys) were harvested for TNF- α , IL-6, and IL-10 evaluation, following the guidelines provided by the ELISA kit manufacturer. To inspect the fluorescence intensity of DiR in the tumors, the harvested tumor tissues were fixed with 4% paraformaldehyde. These fixed tissues were then sectioned and examined under a fluorescence microscope to observe the distribution of DiR. Meanwhile, to further confirm whether MetaCell was intact or entered tumor tissues, MetaCell loading with Lip@Fe-Cu-MOFs_{DiR} was labeled with DiO. Tumor-bearing mice received intravenous administration of double-labeled MetaCell every 2 days, followed by NIR laser irradiation (808 nm, 1.5 W/cm², 5 min) after 24 hours. The tumor tissues were harvested after 7-day administration, fixed, then sectioned, and examined under a fluorescence microscope to observe the distribution of DiR and DiO.

In the context of photothermal imaging, Lip@Fe-Cu-MOFs (administered at a dosage of 10 mg/kg of Fe) or MetaCell (2×10^7 cells per mouse) was injected into 4T1 tumor-bearing mice, respectively. After a 24-hour postinjection period, the mice were subjected to a 5-min laser irradiation (808 nm, 1 W/cm²) after 24 hours of administration. The photothermal images were captured using a thermal imaging camera (CompactPRO, Seek Thermal, USA).

Blood stability of MetaCell

The whole blood was collected from tumor-bearing female BALB/c mice (~100 mm³ of tumor volume) through angular venous puncture using a capillary tube containing a drop of heparin solution. Subsequently, 2×10^7 of MetaCell (containing C6-labeled Lip@Fe-Cu-MOFs) suspended in 100 μ l of PBS was added into the anticoagulant whole blood and incubated for 12 hours at 37°C. The sample was centrifuged at 3000 rpm at 4°C for 5 min at the predetermined time points to analysis fluorescence intensity of C6 (Ex/Em = 465/502 nm) in the serum using a microplate reader.

In vivo antitumor effect of MetaCell

Mice bearing tumors were randomly divided into four groups and administered intravenously with PBS, Lip@Fe-Cu-MOFs (at a dosage of 10 mg/kg of Fe), or MetaCell (2×10^7 cells per mouse). These injections were followed by 808-nm laser irradiation (1.5 W/cm²) for 5 min after 24 hours of injection. This process was repeated every 2 days for a total of eight times. Both the tumor volumes and the body weights of the mice were measured over the course of the 16-day treatment. Following the 16-day treatment, the mice were euthanized, and their tumors and major organs were harvested for further analyses. These analyses included H&E staining, DHE staining, immunostaining for GPX4 and DLAT, or GSH/GSSG analysis. The mice's serum was also collected to measure the levels of AST, ALT, and BUN as markers of liver and kidney functions. In addition to these analyses, the survival rate of the animals was tracked over a 60-day period.

Total RNA from the tumor tissues of each group was extracted using TRIzol reagent and reverse-transcribed into cDNA to investigate the expressions of LIAS and FDX1 using a cDNA RT Kit. The detailed methods of RT-qPCR analysis were as the same of the section mentioned in vitro.

Statistical analysis

All experiments were repeated at least three times. Data are represented as mean \pm SD. Error bars represent SEM from independent samples assayed within the experiments. Statistical analysis was done with GraphPad Prism 6 software. Statistical significance was calculated using two-tailed Student's *t* test or one-way analysis of variance (ANOVA) in Fig. 6C: * represents $P < 0.05$, ** represents $P < 0.01$, and *** represents $P < 0.001$.

Supplementary Materials

This PDF file includes:

Figs. S1 to S19

REFERENCES AND NOTES

- M. A. Zoroddu, J. Aaseth, G. Crisponi, S. Medici, M. Peana, V. M. Nurchi, The essential metals for humans: A brief overview. *J. Inorg. Biochem.* **195**, 120–129 (2019).
- C. Wang, R. Zhang, X. Wei, M. Lv, Z. Jiang, Metalloimmunology: The metal ion-controlled immunity. *Adv. Immunol.* **145**, 187–241 (2020).
- C. T. Chasapis, P. A. Ntoupa, C. A. Spiliopoulou, M. E. Stefanidou, Recent aspects of the effects of zinc on human health. *Arch. Toxicol.* **94**, 1443–1460 (2020).
- M. Bisaglia, L. Bubacco, Copper ions and Parkinson's disease: Why is homeostasis so relevant? *Biomolecules* **10**, 195 (2020).
- S. Gervason, D. Larkem, A. B. Mansour, T. Botzanowski, C. S. Müller, L. Pecqueur, G. L. Pavéc, A. Delaunay-Moisan, O. Brun, J. Agramunt, A. Grandas, M. Fontecave, V. Schünemann, S. Cianféran, C. Sizun, M. B. Tolédano, B. D' Austréaux, Physiologically relevant reconstitution of iron-sulfur cluster biosynthesis uncovers persulfide-processing functions of ferredoxin-2 and frataxin. *Nat. Commun.* **10**, 3566 (2019).
- D. A. da Silva, A. De Luca, R. Squitti, M. Rongioletti, L. Rossi, C. M. L. Machado, G. Cerchiaro, Copper in tumors and the use of copper-based compounds in cancer treatment. *J. Inorg. Biochem.* **226**, 111634 (2022).
- Y. Chen, Z. Fan, Y. Yang, C. Gu, Iron metabolism and its contribution to cancer (Review). *Int. J. Oncol.* **54**, 1143–1154 (2019).
- M. Barbagallo, N. Veronese, L. J. Dominguez, Magnesium in aging, health and diseases. *Nutrients* **13**, 463 (2021).
- E. J. Ge, A. I. Bush, A. Casini, P. A. Cobine, J. R. Cross, G. M. DeNicola, Q. P. Dou, K. J. Franz, V. M. Gohil, S. Gupta, S. G. Kaler, S. Lutsenko, V. Mittal, M. J. Petris, R. Polishchuk, M. Ralle, M. L. Schilsky, N. K. Tonks, L. T. Vahdat, L. Van Aelst, D. Xi, P. Yuan, D. C. Brady, C. J. Chang, Connecting copper and cancer: From transition metal signalling to metalloplasia. *Nat. Rev. Cancer* **22**, 102–113 (2022).
- X. Yao, W. Li, D. Fang, C. Xiao, X. Wu, M. Li, Z. Luo, Emerging roles of energy metabolism in ferroptosis regulation of tumor cells. *Adv. Sci.* **8**, e2100997 (2021).
- X. Sun, Y. Zhang, J. Li, K. S. Park, K. Han, X. Zhou, Y. Xu, J. Nam, J. Xu, X. Shi, L. Wei, Y. L. Lei, J. J. Moon, Amplifying STING activation by cyclic dinucleotide-manganese particles for local and systemic cancer metalloimmunotherapy. *Nat. Nanotechnol.* **16**, 1260–1270 (2021).
- K. Mortezaee, M. Najafi, H. Samadian, H. Barabadi, A. Azarnezhad, A. Ahmadi, Redox interactions and genotoxicity of metal-based nanoparticles: A comprehensive review. *Chem. Biol. Interact.* **312**, 108814 (2019).
- P. Lelièvre, L. Sancey, J.-L. Coll, A. Deniaud, B. Busser, The multifaceted roles of copper in cancer: A trace metal element with dysregulated metabolism, but also a target or a bullet for therapy. *Cancers* **12**, 3594 (2020).
- R. Szabo, C. Bodolea, T. Mocan, Iron, copper, and zinc homeostasis: Physiology, pathophysiology, and nanomediated applications. *Nanomaterials* **11**, 2958 (2021).
- K. J. Franz, N. Metzler-Nolte, Introduction: Metals in medicine. *Chem. Rev.* **119**, 727–729 (2019).
- L. Chen, J. Min, F. Wang, Copper homeostasis and cuproptosis in health and disease. *Signal Transduct. Target. Ther.* **7**, 378 (2022).
- K. Zhang, Z. Ma, S. Li, Y. Wu, J. Zhang, W. Zhang, Y. Zhao, H. Han, Disruption of dual homeostasis by a metal-organic framework nanoreactor for ferroptosis-based immunotherapy of tumor. *Biomaterials* **284**, 121502 (2022).
- S.-R. Li, L.-L. Bu, L. Cai, Cuproptosis: Lipoylated TCA cycle proteins-mediated novel cell death pathway. *Signal Transduct. Target. Ther.* **7**, 158 (2022).
- X. Jiang, B. R. Stockwell, M. Conrad, Ferroptosis: Mechanisms, biology and role in disease. *Nat. Rev. Mol. Cell Biol.* **22**, 266–282 (2021).
- Y. Yu, Y. Yan, F. Niu, Y. Wang, X. Chen, G. Su, Y. Liu, X. Zhao, L. Qian, P. Liu, Y. Xiong, Ferroptosis: A cell death connecting oxidative stress, inflammation and cardiovascular diseases. *Cell Death Discov.* **7**, 193 (2021).
- W. Pi, L. Wu, J. Lu, X. Lin, X. Huang, Z. Wang, Z. Yuan, H. Qiu, J. Zhang, H. Lei, P. Wang, A metal ions-mediated natural small molecules carrier-free injectable hydrogel achieving laser-mediated photo-Fenton-like anticancer therapy by synergy apoptosis/cuproptosis/anti-inflammation. *Bioact. Mater.* **29**, 98–115 (2023).
- P. Tsvetkov, S. Coy, B. Petrova, M. Dreishpoon, A. Verma, M. Abdusamad, J. Rossen, L. Joesch-Cohen, R. Humeidi, R. D. Spangler, J. K. Eaton, E. Frenkel, M. Kocak, S. M. Corsello, S. Lutsenko, N. Kanarek, S. Santagata, T. R. Golub, Copper induces cell death by targeting lipoylated TCA cycle proteins. *Science* **375**, 1254–1261 (2022).
- C. Liang, X. Zhang, M. Yang, X. Dong, Recent progress in ferroptosis inducers for cancer therapy. *Adv. Mater.* **31**, e1904197 (2019).
- J. P. Friedmann Angeli, D. V. Krysko, M. Conrad, Ferroptosis at the crossroads of cancer-acquired drug resistance and immune evasion. *Nat. Rev. Cancer* **19**, 405–414 (2019).
- Y. Lu, Q. Pan, W. Gao, Y. Pu, B. He, Reversal of cisplatin chemotherapy resistance by glutathione-resistant copper-based nanomedicine via cuproptosis. *J. Mater. Chem. B* **10**, 6296–6306 (2022).
- D. Tang, X. Chen, G. Kroemer, Cuproptosis: A copper-triggered modality of mitochondrial cell death. *Cell Res.* **32**, 417–418 (2022).
- X. Tong, R. Tang, M. Xiao, J. Xu, W. Wang, B. Zhang, J. Liu, X. Yu, S. Shi, Targeting cell death pathways for cancer therapy: Recent developments in necroptosis, pyroptosis, ferroptosis, and cuproptosis research. *J. Hematol. Oncol.* **15**, 174 (2022).
- W. Xu, J. Qian, G. Hou, T. Wang, J. Wang, Y. Wang, L. Yang, X. Cui, A. Suo, A hollow amorphous bimetal organic framework for synergistic cuproptosis/ferroptosis/apoptosis anticancer therapy via disrupting intracellular redox homeostasis and copper/iron metabolisms. *Adv. Funct. Mater.* **32**, 2205013 (2022).
- J. Zheng, J. Du, H. Ge, N. Xu, Q. Yao, S. Long, J. Fan, X. Peng, Viscosity-dependent photocatalysis triggers ferroptosis and type-I photodynamic therapy to kill drug-resistant tumors. *Chem. Eng. J.* **449**, 136565 (2022).
- B. Niu, K. Liao, Y. Zhou, T. Wen, G. Quan, X. Pan, C. Wu, Application of glutathione depletion in cancer therapy: Enhanced ROS-based therapy, ferroptosis, and chemotherapy. *Biomaterials* **277**, 121110 (2021).
- Y. Guo, Y. Xu, Q. Bao, C. Shen, D. Ni, P. Hu, J. Shi, Endogenous copper for nanocatalytic oxidative damage and self-protection pathway breakage of cancer. *ACS Nano* **15**, 16286–16297 (2021).
- X. Zhang, S. Lin, F. Zhao, J. Zhang, S. Lei, F. Bai, Q. Liu, J. Wu, T. He, P. Huang, J. Lin, Programmably controllable delivery of metastable ferrous ions for multiscale dynamic imaging guided photothermal primed chemodynamic therapy. *Adv. Mater.* **35**, e2210876 (2023).
- S. Ning, M. Lyu, D. Zhu, J. W. Y. Lam, Q. Huang, T. Zhang, B. Z. Tang, Type-I AIE photosensitizer loaded biomimetic system boosting cuproptosis to inhibit breast cancer metastasis and rechallenge. *ACS Nano* **17**, 10206–10217 (2023).
- M. Amin, T. Lammers, T. L. M. Ten Hagen, Temperature-sensitive polymers to promote heat-triggered drug release from liposomes: Towards bypassing EPR. *Adv. Drug Deliv. Rev.* **189**, 114503 (2022).
- H. Sies, V. V. Belousov, N. S. Chandel, M. J. Davies, D. P. Jones, G. E. Mann, M. P. Murphy, M. Yamamoto, C. Winterbourn, Defining roles of specific reactive oxygen species (ROS) in cell biology and physiology. *Nat. Rev. Mol. Cell Biol.* **23**, 499–515 (2022).
- W. Wang, K. Lu, X. Jiang, Q. Wei, L. Zhu, X. Wang, H. Jin, L. Feng, Ferroptosis inducers enhanced cuproptosis induced by copper ionophores in primary liver cancer. *J. Exp. Clin. Cancer Res.* **42**, 142 (2023).
- M. Yu, F. Guo, F. Tan, N. Li, Dual-targeting nanocarrier system based on thermosensitive liposomes and gold nanorods for cancer thermo-chemotherapy. *J. Control. Release* **215**, 91–100 (2015).
- L. Li, T. L. ten Hagen, D. Schipper, T. M. Wijnberg, G. C. van Rhooon, A. M. Eggermont, L. H. Lindner, G. A. Koning, Triggered content release from optimized stealth thermosensitive liposomes using mild hyperthermia. *J. Control. Release* **143**, 274–279 (2010).
- L. Wu, J. Zhang, W. Watanabe, Physical and chemical stability of drug nanoparticles. *Adv. Drug Deliv. Rev.* **63**, 456–469 (2011).
- W. J. Lokkerse, E. C. Kneepkens, T. L. ten Hagen, A. M. Eggermont, H. Grull, G. A. Koning, In depth study on thermosensitive liposomes: Optimizing formulations for tumor specific therapy and in vitro to in vivo relations. *Biomaterials* **82**, 138–150 (2016).
- T. Ta, T. M. Porter, Thermosensitive liposomes for localized delivery and triggered release of chemotherapy. *J. Control. Release* **169**, 112–125 (2013).
- Q.-X. Huang, J.-L. Liang, Q.-W. Chen, X.-K. Jin, M.-T. Niu, C.-Y. Dong, X.-Z. Zhang, Metal-organic framework nanoagent induces cuproptosis for effective immunotherapy of malignant glioblastoma. *Nano Today* **51**, 101911 (2023).

43. H. Peng, X. Zhang, P. Yang, J. Zhao, W. Zhang, N. Feng, W. Yang, J. Tang, Defect self-assembly of metal-organic framework triggers ferroptosis to overcome resistance. *Bioact. Mater.* **19**, 1–11 (2023).
44. J. Fu, T. Li, Y. Yang, L. Jiang, W. Wang, L. Fu, Y. Zhu, Y. Hao, Activatable nanomedicine for overcoming hypoxia-induced resistance to chemotherapy and inhibiting tumor growth by inducing collaborative apoptosis and ferroptosis in solid tumors. *Biomaterials* **268**, 120537 (2021).
45. S. Koo, O. K. Park, J. Kim, S. I. Han, T. Y. Yoo, N. Lee, Y. G. Kim, H. Kim, C. Lim, J. S. Bae, J. Yoo, D. Kim, S. H. Choi, T. Hyeon, Enhanced chemodynamic therapy by Cu-Fe peroxide nanoparticles: Tumor microenvironment-mediated synergistic Fenton reaction. *ACS Nano* **16**, 2535–2545 (2022).
46. L.-H. Fu, Y. Wan, C. Qi, J. He, C. Li, C. Yang, H. Xu, J. Lin, P. Huang, Nanocatalytic theranostics with glutathione depletion and enhanced reactive oxygen species generation for efficient cancer therapy. *Adv. Mater.* **33**, e2006892 (2021).
47. K. Khalid, X. Tan, H. F. Mohd Zaid, Y. Tao, C. Lye Chew, D. T. Chu, M. K. Lam, Y. C. Ho, J. W. Lim, L. Chin Wei, Advanced in developmental organic and inorganic nanomaterial: A review. *Bioengineered* **11**, 328–355 (2020).
48. S. Tan, T. Wu, D. Zhang, Z. Zhang, Cell or cell membrane-based drug delivery systems. *Theranostics* **5**, 863–881 (2015).
49. Z. Li, Y. Wang, Y. Ding, L. Repp, G. S. Kwon, Q. Hu, Cell-based delivery systems: Emerging carriers for immunotherapy. *Adv. Funct. Mater.* **31**, 2100088 (2021).
50. Y. Chen, D. Qin, J. Zou, X. Li, X. D. Guo, Y. Tang, C. Liu, W. Chen, N. Kong, C. Y. Zhang, W. Tao, Living leukocyte-based drug delivery systems. *Adv. Mater.* **35**, e2207787 (2023).
51. Y. Ding, Y. Wang, Q. Hu, Recent advances in overcoming barriers to cell-based delivery systems for cancer immunotherapy. *Exploration* **2**, 20210106 (2022).
52. V. Mutua, L. J. Gershwin, A Review of neutrophil extracellular traps (NETs) in disease: Potential anti-NETs therapeutics. *Clin. Rev. Allergy Immunol.* **61**, 194–211 (2021).
53. M. A. Giese, L. E. Hind, A. Huttenlocher, Neutrophil plasticity in the tumor microenvironment. *Blood* **133**, 2159–2167 (2019).
54. H. K. Lehman, B. H. Segal, The role of neutrophils in host defense and disease. *J. Allergy Clin. Immunol.* **145**, 1535–1544 (2020).
55. L. Tang, S. He, Y. Yin, H. Liu, J. Hu, J. Cheng, W. Wang, Combination of nanomaterials in cell-based drug delivery systems for cancer treatment. *Pharmaceutics* **13**, 1888 (2021).
56. T. M. Seibt, B. Proneth, M. Conrad, Role of GPX4 in ferroptosis and its pharmacological implication. *Free Radic. Biol. Med.* **133**, 144–152 (2019).
57. M. Gao, J. Yi, J. Zhu, A. M. Minikes, P. Monian, C. B. Thompson, X. Jiang, Role of mitochondria in ferroptosis. *Mol. Cell* **73**, 354–363.e3 (2019).
58. A. M. Battaglia, R. Chirillo, I. Aversa, A. Sacco, F. Costanzo, F. Biamonte, Ferroptosis and cancer: Mitochondria meet the “iron maiden” cell death. *Cells* **9**, 1505 (2020).
59. Z. Li, C. Sun, Z. Qin, Metabolic reprogramming of cancer-associated fibroblasts and its effect on cancer cell reprogramming. *Theranostics* **11**, 8322–8336 (2021).
60. I. H. Bartelink, E. F. Jones, S. K. Shahidi-Latham, P. R. E. Lee, Y. Zheng, P. Vicini, L. van 't Veer, D. Wolf, A. Iagaru, D. L. Kroetz, B. Prideaux, C. Cilliers, G. M. Thurber, Z. Wimana, G. Gebhart, Tumor drug penetration measurements could be the neglected piece of the personalized cancer treatment puzzle. *Clin. Pharmacol. Ther.* **106**, 148–163 (2019).
61. H. Wang, J. Zang, Z. Zhao, Q. Zhang, S. Chen, The advances of neutrophil-derived effective drug delivery systems: A key review of managing tumors and inflammation. *Int. J. Nanomedicine* **16**, 7663–7681 (2021).
62. L. Yvan-Charvet, L. G. Ng, Granulopoiesis and neutrophil homeostasis: A metabolic, daily balancing act. *Trends Immunol.* **40**, 598–612 (2019).
63. S. B. Coffelt, M. D. Wellenstein, K. E. de Visser, Neutrophils in cancer: Neutral no more. *Nat. Rev. Cancer* **16**, 431–446 (2016).
64. M. Wu, H. Zhang, C. Tie, C. Yan, Z. Deng, Q. Wan, X. Liu, F. Yan, H. Zheng, MR imaging tracking of inflammation-activatable engineered neutrophils for targeted therapy of surgically treated glioma. *Nat. Commun.* **9**, 4777 (2018).
65. J. Che, A. Najer, A. K. Blakney, P. F. McKay, M. Bellahcene, C. W. Winter, A. Sintou, J. Tang, T. J. Keane, M. D. Schneider, R. J. Shattock, S. Sattler, M. M. Stevens, Neutrophils enable local and non-invasive liposome delivery to inflamed skeletal muscle and ischemic heart. *Adv. Mater.* **32**, e2003598 (2020).
66. M. R. Williams, V. Azcutia, G. Newton, P. Alcaide, F. W. Lusinskas, Emerging mechanisms of neutrophil recruitment across endothelium. *Trends Immunol.* **32**, 461–469 (2011).
67. Z. Feng, J. Yang, L. Zhu, T. Sun, Bromine functionalized Fe/Cu bimetallic MOFs for accelerating Fe (III)/Fe (II) cycle and efficient degradation of phenol in Fenton-like system. *Colloids Surfaces A* **658**, 130701 (2023).
68. Y. Xu, X. Zhang, G. Hu, X. Wu, Y. Nie, H. Wu, D. Kong, X. Ning, Multistage targeted “Photoactive neutrophil” for enhancing synergistic photo-chemotherapy. *Biomaterials* **279**, 121224 (2021).

Acknowledgments

Funding: This work was supported by the following listed fundings: National Key Research and Development Program of China 2021YFF1000700, 2019YFA0802800, and 2018YFB1105400 (X.N.), National Natural Science Foundation of China 21472090 (X.N.) and 32301148 (Y.X.), Natural Science Foundation of Jiangsu Province BK20180334 (X.N.), Fundamental Research Funds for Central Universities Nanjing University (X.N.), Key Research and Development Program of Jiangsu Provincial Department of Science and Technology of China BE2019002 (X.N.), and Jiangsu Funding Program for Excellent Postdoctoral Talent 2023ZB486 (K.C.) and 202202B23 (Y.X.). **Author contributions:** Conceptualization: Y.X. and X.N. Methodology: K.C., A.Z., X.Z., and J.H. Investigation: Y.X., K.C., and X.Z. Visualization: K.C. and X.Z. Supervision: A.Z. and Y.X. Writing—original draft: K.C. Writing—review and editing: X.N. and A.Z. **Competing interests:** The authors declare that they have no competing interests. **Data and materials availability:** All data needed to evaluate the conclusions in the paper are present in the paper and/or the Supplementary Materials.

Submitted 16 August 2023

Accepted 5 March 2024

Published 10 April 2024

10.1126/sciadv.adk3201